

THS

# This is to certify that the thesis entitled

#### NUMERICAL SIMULATION OF AIRFLOW IN THE EQUINE UPPER AIRWAY TO STUDY THE PHENOMENON OF DORSAL DISPLACEMENT OF SOFT PALATE

presented by

#### SRIKANTH SRIDHAR

has been accepted towards fulfillment of the requirements for the

M.S. degree in MECHANICAL ENGINEERING

Major Professor's Signature

Date

LIBRARY Michigan State University

# PLACE IN RETURN BOX to remove this checkout from your record. TO AVOID FINES return on or before date due. MAY BE RECALLED with earlier due date if requested.

DATE DUE	DATE DUE	DATE DUE

6/07 p:/CIRC/DateDue.indd-p.1

# NUMERICAL SIMULATION OF AIRFLOW IN THE EQUINE UPPER AIRWAY TO STUDY THE PHENOMENON OF DORSAL DISPLACEMENT OF SOFT PALATE

Ву

Srikanth Sridhar

#### A THESIS

Submitted to
Michigan State University
in partial fulfillment of the requirements
for the degree of

MASTER OF SCIENCE

Department of Mechanical Engineering

2008

#### ABSTRACT

# NUMERICAL SIMULATION OF AIRFLOW IN THE EQUINE UPPER AIRWAY TO STUDY THE PHENOMENON OF DORSAL DISPLACEMENT OF SOFT PALATE

By

#### Srikanth Sridhar

Dorsal Displacement of Soft Palate (DDSP) is a commonly observed upper-airway respiratory disorder in horses, especially while racing. Either solely or in combination with other conditions, DDSP is one of the most common causes for performance retardation and abnormal respiratory noise in equine athletes. However, the exact causes for the occurrence of DDSP are not yet understood clearly. Besides, little is known about the dynamic pressure and velocity distributions that may contribute to dynamic collapse of the soft palate into the upper airway.

In this work, the airflow through the equine upper airway was studied using Computational Fluid Dynamics in order to investigate if there is correlation between a particular flow regime and the occurrence of DDSP. Post-mortem CT scan images of the upper airway were used to develop a computational domain for the upper airway geometry. Numerical computations were performed in order to solve the flow field for different geometries and breathing conditions. The results of the numerical solutions were validated by comparing with experimental results recorded in literature. Pressure and velocity distributions were studied throughout the domain and throughout the breathing cycle in order to find out if there is a correlation between the flow field and the occurrence of DDSP. The various assumptions applied to the modeling were discussed.

### **ACKNOWLEDGMENTS**

I take this opportunity to thank my thesis advisor Dr. Mei Zhuang for her guidance with this work and more importantly, for her patience, kindness and generosity of spirit. I appreciate her knowledge and skill in the field of fluid mechanics. She has been a constant source of encouragement and support, even at those times when I had fallen short of her expectations.

I'd also like to thank Dr. N. Edward Robinson (College of Veterinary Medicine, MSU). In addition to providing partial funding for this work and co-guiding this thesis, he has also generously shared with me, gems from his vast treasure of knowledge and experience in the a wide spectrum of fields ranging from biology to music! I hold great appreciation for his fervor for knowledge and passion for science and science-teaching.

I thank Dr. Frederik Derksen (College of Veterinary Medicine, MSU) for his guidance with this work and for not getting annoyed with my endless questions to him on equine respiratory physiology, but answering them with patience.

The airway geometries used in this work were from Dr. Rob Malinowski (College of Veterinary Medicine, MSU). I thank him for spending his time in developing the airway models and sharing his valuable insights. I greatly admire his skill with computers!

The assistance provided by Ms. Diana Rosenstein and Ms. Maggie Hofmann (College of Veterinary Medicine) in developing the airway models is greatly appreciated.

I'd like thank Aida Montalvo (Graduate Secretary, Department of Mechanical Engineering) for all her help throughout my stay at MSU. Her secretarial skills, experience and communication ability have saved me lot of time, effort and energy.

Dr. Farhad Jaberi (Department of Mechanical Engineering, MSU), and Dr. Charles Petty (Department of Chemical Engineering, MSU) are greatly appreciated for sharing their valuable insights on turbulence modeling. Dr. Jaberi was one of the members of the thesis committee.

I thank my family, friends and my lab-mates at the CFD lab, MSU for their moral support. In particular, I'm very grateful to my friends Deebika and Saravan for having helped me complete my thesis in several ways, including proof-reading and offering their comments.

# **TABLE OF CONTENTS**

LIST OF TABLES	
LIST OF FIGURES	vii
Chapter 1: Introduction	
1.1. Dorsal Displacement of Soft Palate	
1.2. CFD and its application to modeling respiratory flows	
1.3. Scope of the work	
1.4. Organization of the thesis	4
Chapter 2: Problem Description	
2.1. Description of DDSP	
2.2. Nature of flow within the upper airway	6
2.3. Problem statement	7
Chapter 3: Method	8
3.1. The upper airway model	8
3.1.1. Computational domain corresponding to the upper airway	8
3.1.2. Manipulating the upper airway geometry	10
3.1.3. Pre-processing and Meshing	13
3.2. Mathematical formulation	17
3.2.1. Governing equations	17
3.2.2. Boundary conditions	19
3.2.3. Initial condition	
3.3. Numerical solution methods	
3.4. Choice of turbulence model	
3.5. Assumptions in modeling	33
Chapter 4: Results and Discussion	35
4.1. Validation	35
4.2. Velocity and pressure distributions:	37
4.2.1 Velocity and Pressure distributions through the tracheal pressure cycle	37
4.2.1. Variation in velocity distribution with respiratory rate	50
4.2.2. Variation of velocity distribution with flexure in upper airway	
4.3. Wall pressure along the dorsal surface of lower wall	
4.3.1. Variation of wall pressure distribution with respiratory rate	
4.3.2. Variation of wall pressure distribution with induced flexure in the upper airway	
Chapter 5: Conclusions and Future Work	
References	

# LIST OF TABLES

Unsteady pressure boundary condition corresponding to different rates of respiration	•	
Comparison between experimental and numerical results		

# **LIST OF FIGURES**

## IMAGES IN THIS THESIS ARE PRESENTED IN COLOR

Figure 2.1. Sagittal sectional view of equine upper airway
Figure 3.1. Image from CT scan of upper airway
Figure 3.2. Two-dimensional model developed from CT scan
Figure 3.3. Model representing airway with no induced flexure
Figure 3.4. Model representing airway with mild induced flexure
Figure 3.5. Model representing airway with extreme induced flexure
Figure 3.6. Boundaries and zones during inhalation
Figure 3.7. Boundaries and zones during exhalation
Figure 3.8. Velocity gradient based adaptive refinement of mesh
Figure 3.9. Generic boundary conditions for respiratory flow
Figure 3.10. Tracheal pressure cycle during rest
Figure 3.11. Tracheal pressure cycle during mild exercise
Figure 3.12. Tracheal pressure cycle during intense exercise
Figure 3.13. Locations of test points within the domain for monitoring solutions 26
Figure 3.14. Variation of pressure with respect to time at the test point 'a' indicated in Figure 3.13
Figure 3.15. Variation of x-velocity with respect to time at the test point 'b' indicated in Figure 3.13
Figure 3.16. Locations of test surfaces within the computational domain for comparing solutions obtained using different models

Figure 3.17.	Comparison between k-epsilon, k-omega and RSM model based solutions velocity profile at cross-section B1-B2	
Figure 3.18.	Orientation of the coordinate axes within the domain	
	Velocity distribution (m/s) at peak inspiration	
	Occurrence of peak inspiration relative to the tracheal pressure cycle	
_	Pressure contours (Pa) at peak inspiration	
_	Occurrence of peak inspiration relative to the tracheal pressure cycle	
_	Velocity distribution (m/s) at end of inspiration and just before expiration	
	Occurrence of end of inspiration relative to the tracheal pressure cycle	
Figure 4.7. P	Pressure contours (Pa) at end of inspiration and just before expiration	43
Figure 4.8. C	Occurrence of end of inspiration relative to the tracheal pressure cycle	43
Figure 4.9. V	Velocity distribution (m/s) at peak expiration	45
Figure 4.10.	Occurrence of peak expiration relative to the tracheal pressure cycle	45
Figure 4.11.	Pressure contours (Pa) at peak expiration	46
Figure 4.12.	Occurrence of peak expiration relative to the tracheal pressure cycle	46
Figure 4.13.	Velocity distribution (m/s) at end of expiration and just before inspiration	48
Figure 4.14.	Occurrence of end of expiration relative to the tracheal pressure cycle	48
Figure 4.15.	Pressure contours (Pa) at end of expiration and just before inspiration	49
Figure 4.16.	Occurrence of end of expiration relative to the tracheal pressure cycle	49
Figure 4.17.	Velocity distribution (m/s) at end of inspiration - rest condition	51
Figure 4.18.	Velocity distribution (m/s) at end of inspiration - mild exercise condition.	51
Figure 4.19.	Velocity distribution (m/s) at end of inspiration - intense exercise condition	
Figure 4.20.	Velocity distribution (m/s) at end of inspiration – no induced flexure	

Figure 4.21.	Velocity distribution (m/s) at end of inspiration – mild induced flexure 54
Figure 4.22.	Velocity distribution (m/s) at end of inspiration – extreme induced flexure 54
Figure 4.23.	Wall pressure along dorsal surface - variation through the tracheal pressure cycle
Figure 4.24.	Wall pressure along dorsal surface – variation with rate of respiration 58
Figure 4.25.	Wall pressure along dorsal surface – variation with induced flexure 59

# **CHAPTER 1: INTRODUCTION**

In this work, Computational Fluid Dynamics (CFD) was applied to predict the unsteady pressure and velocity distributions within the equine upper airway, corresponding to a set of different respiratory conditions. The motivation behind this work was to determine in what way the pattern of airflow established within the upper airway influences the development of Dorsal Displacement of Soft Palate (DDSP) which is a common performance-retarding respiratory disorder in equine athletes.

This chapter first introduces the reader to the condition of Dorsal Displacement of Soft Palate in horses. This is followed by a very brief introduction to Computational Fluid Dynamics and a crisp overview, with examples, of the application of CFD to modeling biological flows. Finally, the organization of this thesis is concisely described.

# 1.1. Dorsal Displacement of Soft Palate

Dorsal Displacement of the Soft Palate which is commonly referred as 'DDSP' is a common upper airway respiratory disorder that manifests in horses, most often, during intense exercise [1]. In a horse exhibiting this condition the soft palate within the upper airway whose caudal end (or the end in the direction toward the animal's tail), which is usually held in position by the epiglottis muscles is dynamically displaced dorsally (toward the animal's back) into the upper airway, typically during intense exercise. DDSP results in a dynamic obstruction to airflow, particularly during expiration [2], and

is often associated with exercise intolerance and/or abnormal respiratory noise [3]. Intermittent DDSP, either solely or in combination with other disorders is one of the most common causes for poor performance and exercise intolerance in equine athletes [4]. Hence it is important to study the problem and investigate its causes. However, the fact that this condition, quite often, manifests itself only during exercise while without a clinical sign while resting, poses a special challenge for diagnosis and treatment. It is evident from literature that multiple, often interrelated factors, may contribute to DDSP including dysfunction of the epiglottis [5], skeletal muscles [6], and nerves [7].

A few researchers had hypothesized that the fluid mechanics in the equine upper airway may be contributing to DDSP. For instance, Robinson *et al.* [8] suggested negative inspiratory pressures in the pharynx may be a cause for DDSP. However, Rehder *et al.* [9] measured dynamic upper airway pressures and correlated the data with results from endoscopic examination in exercising horses. Based on this, they disagreed that there is a link between the magnitude of negative inspiratory pharyngeal pressures and occurrence of DDSP. Currently, little is known about the distributions of unsteady pressures and velocities inside the upper airway which might be contributing to this condition. Hence it is worthwhile to study the mechanics of flow behind this problem in order to investigate if there is a link.

# 1.2. CFD and its application to modeling respiratory flows

Computational Fluid Dynamics (CFD) is a technique wherein the complex partial differential equations governing the parameters of a flow field are approximated to sets of algebraic equations that are solved using specialized numerical techniques to solve for the unknown flow parameters. There have been several instances where researchers have used CFD to successfully predict the unknown respiratory flow parameters. For instance, Kepler *et al.* [10] successfully predicted and validated with experimental results, the nasal airflow and gas uptake patterns in rhesus monkey by using CFD simulations, while Kimbell et al. [11], predicted flow-dependent nasal uptake patterns of formaldehyde in rat, rhesus monkey and human nasal passages. CFD simulations can not only facilitate analysis by experimentation, but can also be a vital tool in situations where experimentation is not feasible or when the accuracy of experimental results is not within acceptable limits. Moreover, with a computer model to represent the physical problem, changes in the analysis can be easily incorporated by altering the corresponding features of the computer model, obviating lengthy experimental set ups.

# 1.3. Scope of the work

The objective of this work was, to solve the flow field inside the equine upper airway in order to study the distribution of flow parameters such as velocity and pressure on order to investigate whether there is a possible correlation to the occurrence of DDSP. In

particular, it was desired to study the effect of the following on the distribution of flow parameters:

- 1. Intensity/ Rate of respiration
- 2. Flexure in the airway (which is frequently linked with increase in the respiratory rate)

# 1.4. Organization of the thesis

A detailed description of the problem is provided in Chapter 2 along with a description of the nature of the flow within the upper airway. Chapter 3 elaborates the methods followed in this work, beginning with creating the upper airway model. The mathematical formulation, the governing equations solved, turbulence model applied and the numerical solution techniques used for solving them are presented. The assumptions applied to the approach are also described. In chapter 4, the results obtained and their validation details are discussed in detail. Finally, conclusions based on our results are presented.

#### **CHAPTER 2: PROBLEM DESCRIPTION**

This chapter describes the problem of this thesis in detail.

#### 2.1. Description of DDSP

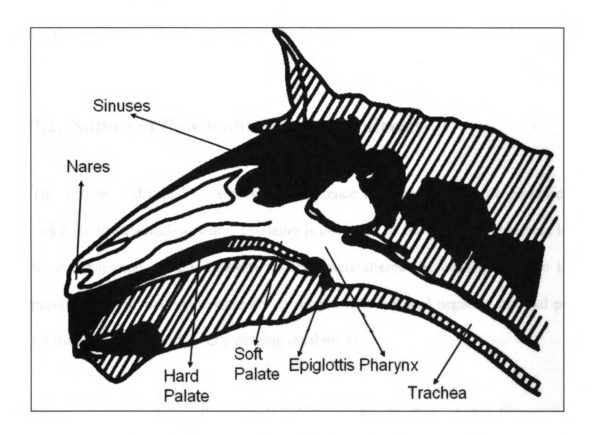


Figure 2.1. Sagittal sectional view of equine upper airway

Figure 2.1 depicts upper airway comprising of the nasal cavity, hard palate, soft palate, epiglottis and the pharynx. A portion of the lower airway (trachea) is also shown in the Figure. The locations of the hard and the soft palates, the epiglottis and the trachea are to be noted. The soft palate, as the name suggests is pliant and, except during swallowing is

kept beneath the epiglottis by muscular activity. Unlike humans, horses cannot breathe through their mouth. The epiglottis acts as a control valve opening the rear of the mouth either solely into the trachea (as in the Figure) while breathing or solely into the esophagus (while swallowing). When DDSP occurs during breathing, the soft palate displaces above the epiglottis and into the airway, obstructing expiratory air coming from the trachea, allowing a portion of the expiratory air into the mouth, thereby vibrating the palate resulting in a loud expiratory noise [12].

# 2.2. Nature of flow within the upper airway

The airflow is driven by the pressure difference between atmospheric pressure at the nares and the tracheal pressure. The latter is governed by the oscillating pressure induced by the diaphragm which expands and contracts alternately, causing positive tracheal pressure for one half-cycle (thereby causing exhalation) and negative tracheal pressure for the next half-cycle (thereby causing inhalation).

Experiments recorded in literature [13] indicate that the flow, during intense exercise, ranges from transition-to-turbulent to fully turbulent. The flow is three dimensional and unsteady since it's driven by an unsteady pressure difference. Since air is a highly compressible fluid, and since the flow is achieved by forcing oscillatory pressures, the flow is expected to exhibit some compressibility effects even though the velocities are expected to be far lesser when compared to that of sound.

The frequency of these time-periodic flows is governed by the forcing pressure's frequency. Low frequencies and amplitudes characterize resting conditions and higher frequencies and amplitudes characterize exercising conditions.

Due to the pulling of reins on the horse, typically while racing, there is expected to be an artificially induced flexure in the upper airway near the pharynx. This additional flexure at the pharyngeal cavity could have a bearing on the flow parameters within the whole of the domain.

# 2.3. Problem statement

The statement of the problem was:

- To solve the flow field within the domain of the upper airway for various respiratory rates and flexure angles.
- 2. To study and understand the distribution of the flow parameters for these different cases.
- 3. To investigate if the results obtained could indicate that the mechanics of the flow contributes to Dorsal Displacement of Soft Palate.

# **CHAPTER 3: METHOD**

In this chapter, the steps involved in the work, beginning with obtaining the geometric model representing the upper airway to solving the flow within the domain, applying the appropriate boundary conditions are described in detail. A detailed description of the mathematical modeling applied to this problem, the numerical techniques used and the simplifying assumptions incorporated are also included.

# 3.1. The upper airway model

The first part of this section describes the development of the computational domain representing the upper airway. The next part elaborates the manipulation of the geometry to obtain models corresponding to different degrees of induced flexures. A description of the schemes used for meshing these domains is described in the last section.

## 3.1.1. Computational domain corresponding to the upper airway

In order to obtain a representative geometry for the upper airway, a post-mortem CT scan was performed on a 15 year old, mixed breed horse. The horse was euthanized for other reasons. The CT scan generated images of the transverse section of the horse's upper airway. These images were stored in the 'dicom' format, which one of the standard formats for medical images from CT. The images were imported into the MPR (Multi-Planar Reconstruction) module of the program called ANALYZE 6.0 (Mayo Clinic). This

program generated two-dimensional images of the sagittal and rostral sections from the transverse section images generated by CT scan. In **Figure 3.1** one such CT scan image which is used to obtain the sagittal section of the upper airway is shown.

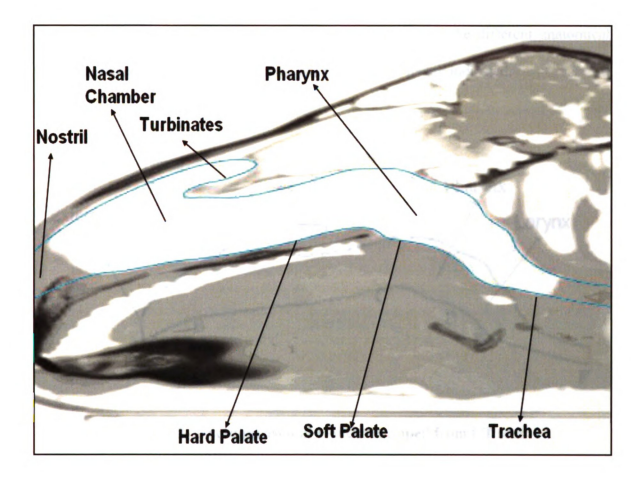


Figure 3.1. Image from CT scan of upper airway

The sagittal section images were saved in 'tiff' format and exported to Adobe Illustrator.

This program traced the sagittal section images and generated the vector format, consisting of points and lines and saved the data in '.ai' format.

Finally, the program 3DS Max (AutoDesk) converted the vector format data to IGES format and scaled to appropriate dimensions. This data can now be imported into GAMBIT (Fluent Inc.) for meshing and other pre-processing activities. **Figure 3.2** shows the image of sagittal section of the upper airway reconstructed from the CT scan data using the procedure mentioned above. The location of the different anatomical features – nares, nasal cavity, turbinates, pharynx and larynx are indicated.

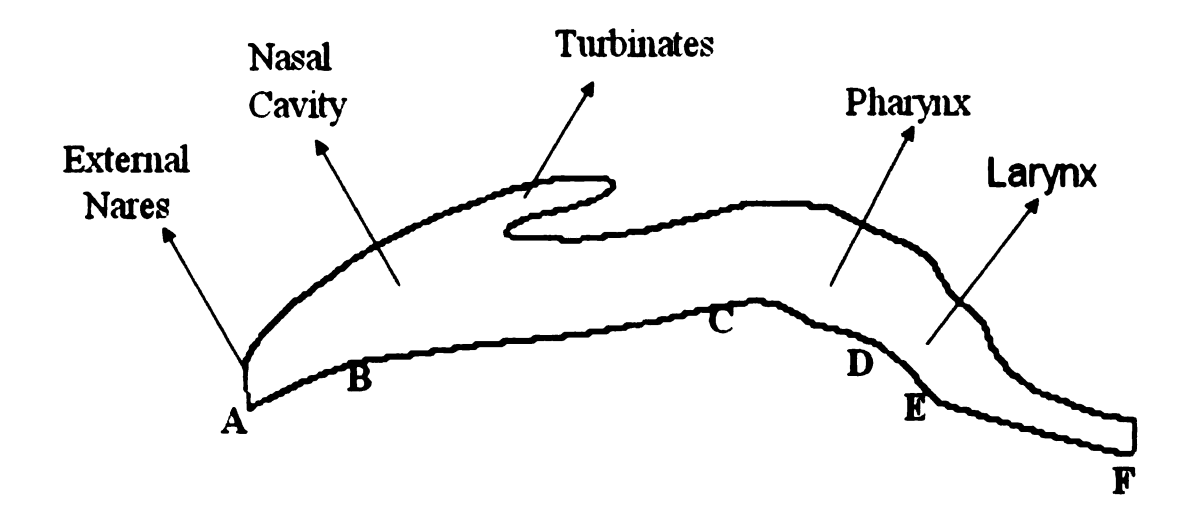


Figure 3.2. Two-dimensional model developed from CT scan

# 3.1.2. Manipulating the upper airway geometry

As mentioned earlier, one of the objectives of this study was to study the effects of the artificial flexure induced in the upper airway. In order to solve the flow field corresponding to these conditions, it is needed to develop the corresponding computational domains. In order to achieve this, the '3DS Max' program was used to manipulate the geometry to create models representing different degrees of flexure in the

upper airway, keeping in mind to not alter the relative positions of the anatomical features. Hence from the original upper airway 2D model described in **Figure 3.2** and **Figure 3.3**, two additional models were thus created representing slightly flexed and extremely flexed airways. The models were flexed around the pharynx as shown in **Figure 3.4** and **Figure 3.5**. These geometries represent the flexing of the upper airway which is induced by pulling of reins on a horse, while racing. The flow field would be solved later on, within each of these domains, corresponding to identical sets of boundary conditions.

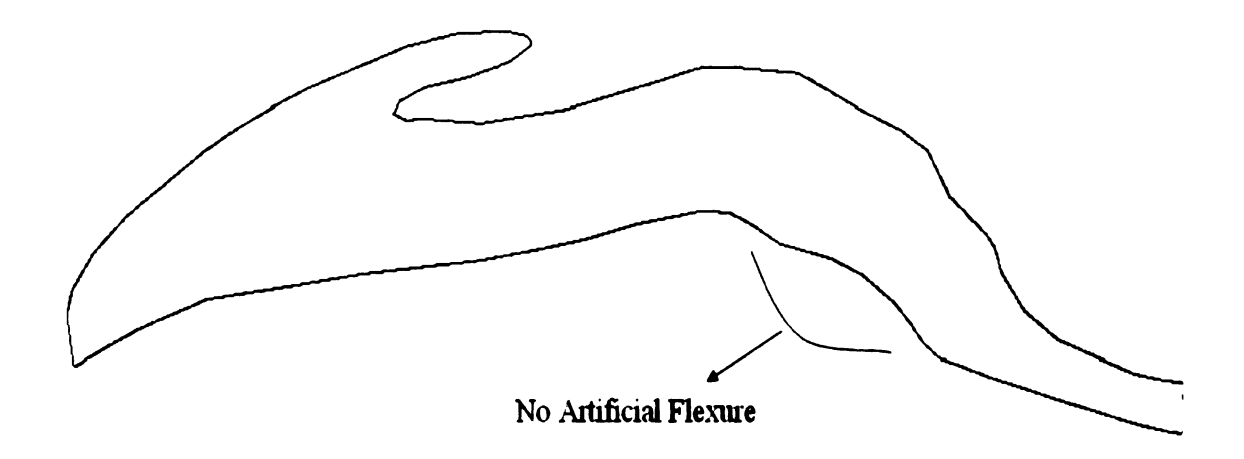


Figure 3.3. Model representing airway with no induced flexure

. 11

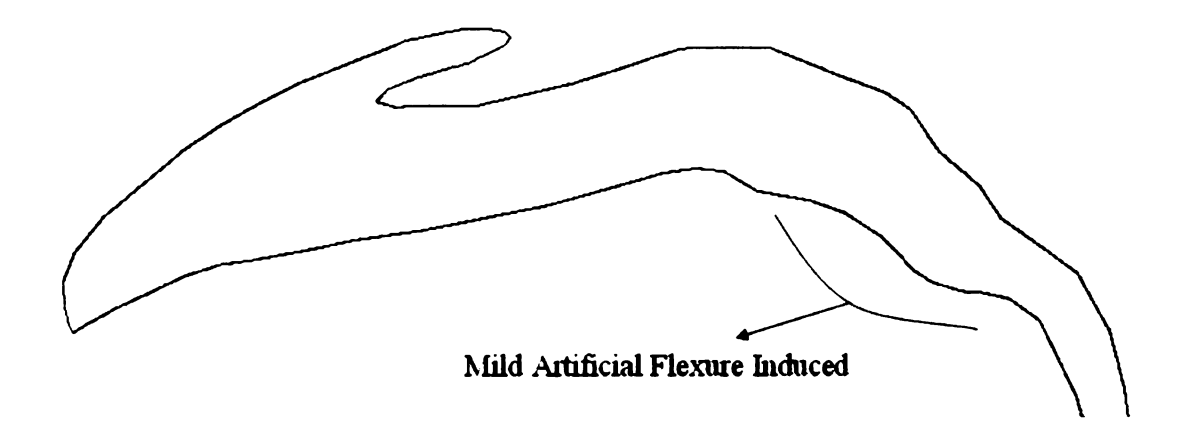


Figure 3.4. Model representing airway with mild induced flexure

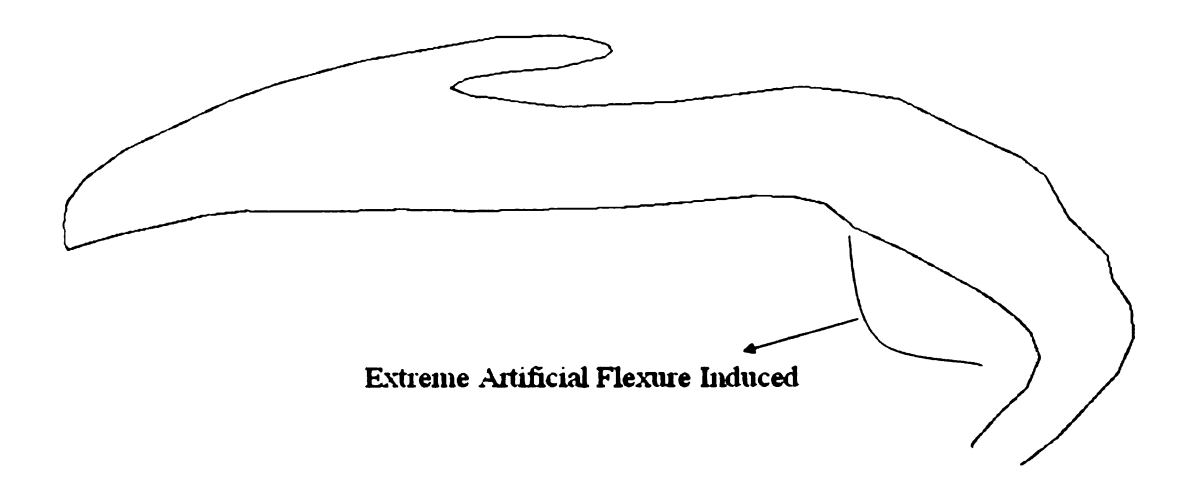


Figure 3.5. Model representing airway with extreme induced flexure

### 3.1.3. Pre-Processing and Meshing

The pre-processing activities that are needed to be performed in order to prepare for the solving the flow field, are described in this section. Firstly, the IGES data files described in the previous section were imported into GAMBIT 2.3.16 (Fluent Inc.). The edges in the two-dimensional model corresponding to different zones, viz. inlet, outlet, walls were defined. This is needed to be done so that the appropriate boundary conditions can be applied to the different zones. The upper and lower boundaries of the geometry were set as no slip wall zones. The left (nostril) and the right (tracheal opening) boundaries were defined as inlet/outlet zones. During inhalation, the nostril boundary would be an inlet and the tracheal opening boundary would be an outlet as shown in **Figure 3.6**.

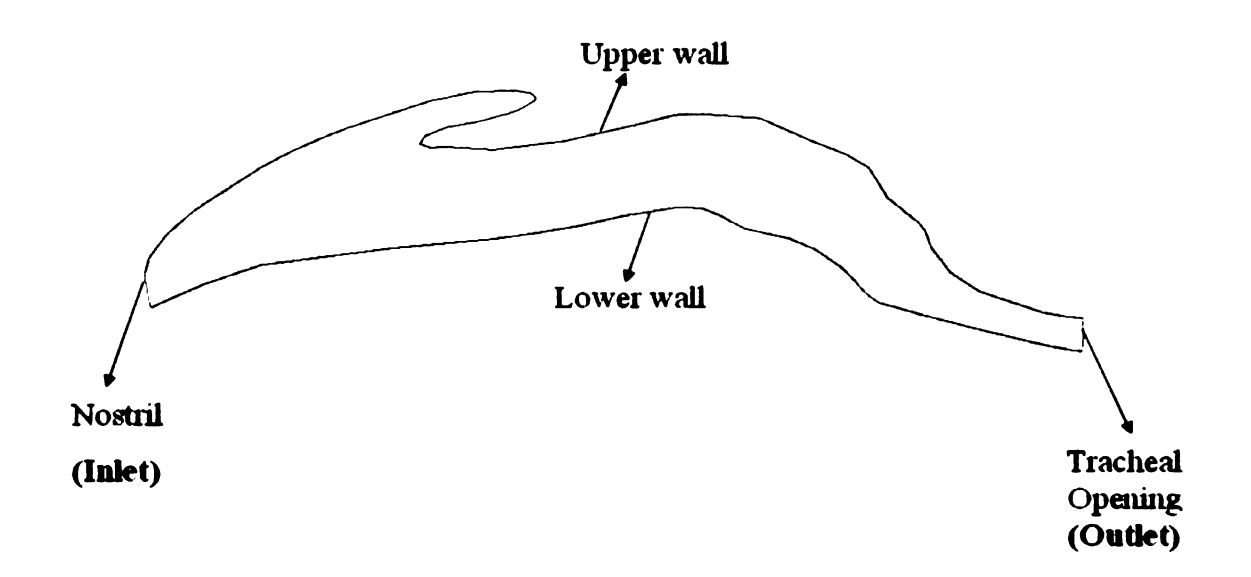


Figure 3.6. Boundaries and zones during inhalation

And during exhalation, the tracheal opening boundary would be an inlet and the nostril boundary would be an outlet as shown in **Figure 3.7**. The pressure difference between the nostril boundary and the tracheal opening boundary would govern the flow direction.

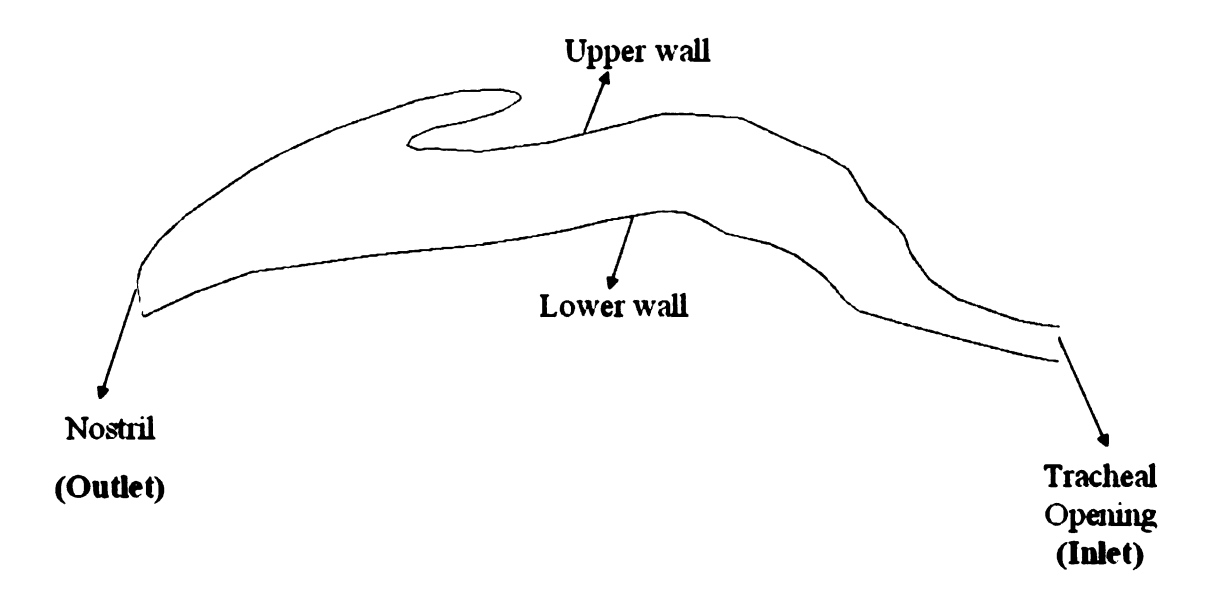


Figure 3.7. Boundaries and zones during exhalation

Once the different zones are defined it's needed to divide the domain into a finite number of tiny cells. This operation, known as meshing and is needed to be done so that the partial differential equations governing the flow of the fluid continuum can be approximated into sets of algebraic equations solved at the discrete nodes introduced by the meshing. The physical domain's extents are of the order 70 cm x 20 cm. (Since the anatomical structures do not fit regular geometric shapes, it is not possible to specify the exact extents in each coordinate direction). The area of the domain corresponding to the non flexed model was about  $4.5 \times 10^{-2} \,\mathrm{m}^2$ . The domain was meshed with an unstructured meshing scheme by paving quadrilateral elements. Due to the irregular shape of the anatomical structures, structured meshing was not appropriate for this situation.

The size of the quadrilateral elements chosen determined the mesh density. An initial mesh size of 0.005 m was selected. The solution obtained for this mesh density was recorded. (A steady-state problem was solved for this purpose, with inlet pressure at atmospheric pressure and the outlet pressure at the maximal diaphragm pressure during extreme exercise.) Then, the mesh was progressively refined and the solutions obtained thereby were compared with the earlier solution(s) in order to check for grid independence. At a mesh size of 0.0005 m, the solution was more or less independent of the grid. All the models were meshed with this same density. And for this mesh density, the number of quadrilateral elements throughout the domain was of the order of 100,000.

In order to adequately resolve the regions with high velocity gradients, a steady state solution was obtained, corresponding to the maximal inspiratory flow rate during intense exercise and grid adaptation, based on velocity gradients was at this particular solution. It was assumed that the maximal velocity gradients would exist in during peak inspiration and hence would require the maximal spatial resolution of grid, representing a "worst-case scenario". The mesh was progressively refined in the same way until a gradual change in mesh density from the walls to the center of the streamline was observed.

Figure 3.8 illustrates this process of adaptive grid refinement that resulted in a finer mesh density near the walls and other regions of high velocity gradients than those of gradual variations in velocity. In addition, after each refinement, the mesh quality was examined by checking the variation in diagonal ratio between adjacent elements throughout the domain and was thus refined.

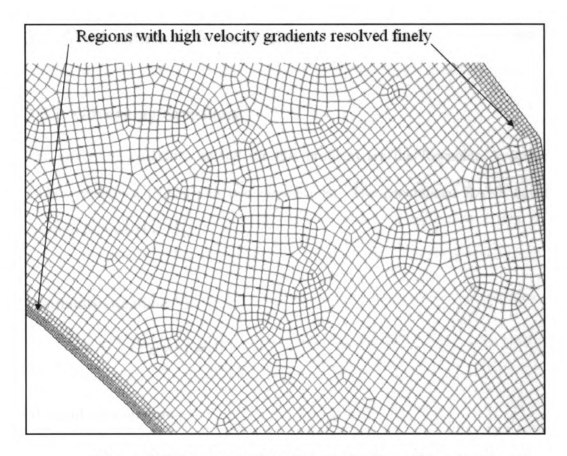


Figure 3.8. Velocity gradient based adaptive refinement of mesh

The mesh thus obtained was saved and exported to the FLUENT program which was used to solve the governing equations for the problem.

## 3.2. Mathematical formulation

### 3.2.1. Governing equations

The governing equations solved for this problem are the Reynolds Averaged Navier Stokes Equations (RANS) in two dimensions. The generalized RANS equations are given as follows [14, 15]:

#### Continuity equation:

$$\frac{\partial \langle \rho \rangle}{\partial t} + \nabla \cdot (\langle \rho \, \boldsymbol{v} \rangle) = 0 \tag{3.1}$$

#### Momentum equation:

$$\frac{\partial \langle \mathbf{v} \rangle}{\partial t} + \nabla \cdot (\langle \rho \, \mathbf{v} \, \mathbf{v} \rangle) = -\nabla \langle \mathbf{p} \rangle + \nabla \cdot (\langle \underline{\tau} \rangle - \langle \rho \, \mathbf{v'} \, \mathbf{v'} \rangle) \tag{3.2}$$

#### **Energy equation:**

$$\frac{\partial \langle C_p T \rangle}{\partial t} + \nabla \cdot (\langle \rho C_p T v \rangle) = \frac{\partial \langle p \rangle}{\partial t} + \frac{1}{\langle \rho \rangle} \langle \rho v \rangle \cdot \nabla \langle p \rangle + \langle v' \cdot \nabla p \rangle + \langle \Phi \rangle$$
(3.3)

Where

$$\langle \Phi \rangle = \langle \tau_{ij} \, \frac{\partial v_i}{\partial x_j} \rangle \tag{3.4}$$

The k-epsilon model, which belongs to the broader class of Two-equation models, is used to introduce to achieve the closure for the  $\langle \rho v' v' \rangle$  term in the momentum equation, which is also known as the Reynolds Stress term.

According to this method, in addition to the RANS equations, two other equations are solved. Each of these equations conserve one additional scalar introduced in order to close the Reynolds stress term. The additional scalar quantities that are introduced are turbulent kinetic energy (k) and Turbulent Kinetic Energy Dissipation Rate (E). The following are the two additional conservation equations introduced because of the k-E turbulence model [15, 16]:

#### k-equation:

$$\frac{\partial (\rho \mathbf{k})}{\partial t} + \nabla \cdot (\rho \mathbf{k} \mathbf{v}) = \nabla \cdot [(\mu + \frac{\mu_t}{\sigma_k}) \nabla k] + G_k + G_b - \rho \varepsilon - Y_M + S_k$$
(3.5)

ε-equation:

$$\frac{\partial (\rho \varepsilon)}{\partial t} + \nabla \cdot (\rho \varepsilon v) = \nabla \cdot \left[ (\mu + \frac{\mu_t}{\sigma_{\varepsilon}}) \nabla \varepsilon \right] + C_{1_{\varepsilon}} \frac{\varepsilon}{k} (G_k + C_{3_{\varepsilon}} G_b) - C_{2_{\varepsilon}} \rho \frac{\varepsilon^2}{k} + S_{\varepsilon}$$
(3.6)

where,

$$C_{\mu} = 0.09$$

$$C_{\varepsilon_1} = 1.44$$

$$C_{\varepsilon_2} = 1.92$$

$$\sigma_k = 1.0$$

$$\sigma_{\varepsilon} = 1.3$$

 $G_k$  and  $G_b$  represent the changes in turbulent kinetic energy due to mean velocity gradients and due to buoyancy respectively.  $Y_M$  represents the contribution of the fluctuating dilatation to the overall dissipation rate [16].  $S_k$  and  $S_\epsilon$  represent source terms. K and epsilon are related by the following equation:

$$\mu_t = \rho C_\mu \frac{k^2}{\varepsilon} \tag{3.7}$$

Finally, the closure is obtained as follows by applying the turbulent-viscosity hypothesis:

$$-\rho \langle v'_{i} v'_{j} \rangle + \frac{2}{3} \rho k \delta_{ij} = 2 \rho \mu_{t} \left( \frac{\partial \langle v_{i} \rangle}{\partial x_{j}} + \frac{\partial \langle v_{j} \rangle}{\partial x_{i}} \right)$$
(3.8)

# 3.2.2. Boundary conditions

The flow within the domain is driven by the pressure difference between the tracheal opening and the nostril. The nostril is at atmospheric pressure and the pressure at the tracheal opening is an unsteady pressure induced by the cyclic expanding and contracting action of the lungs which in turn is achieved by the work done by the muscles of the diaphragm. At the nostril, the pressure was set as atmospheric pressure at sea level and room temperature. At the tracheal end of the upper airway, a sinusoidal oscillating pressure was applied. Although the functional form of the unsteady tracheal pressure is not known, the sinusoidal function with amplitude equal to the peak tracheal pressure and

frequency equal to breath frequency was assumed to be a suitable approximation. At all the wall zones, the no-slip boundary condition was applied. A generic illustration of the boundary conditions applied to this problem is shown in **Figure 3.9**.

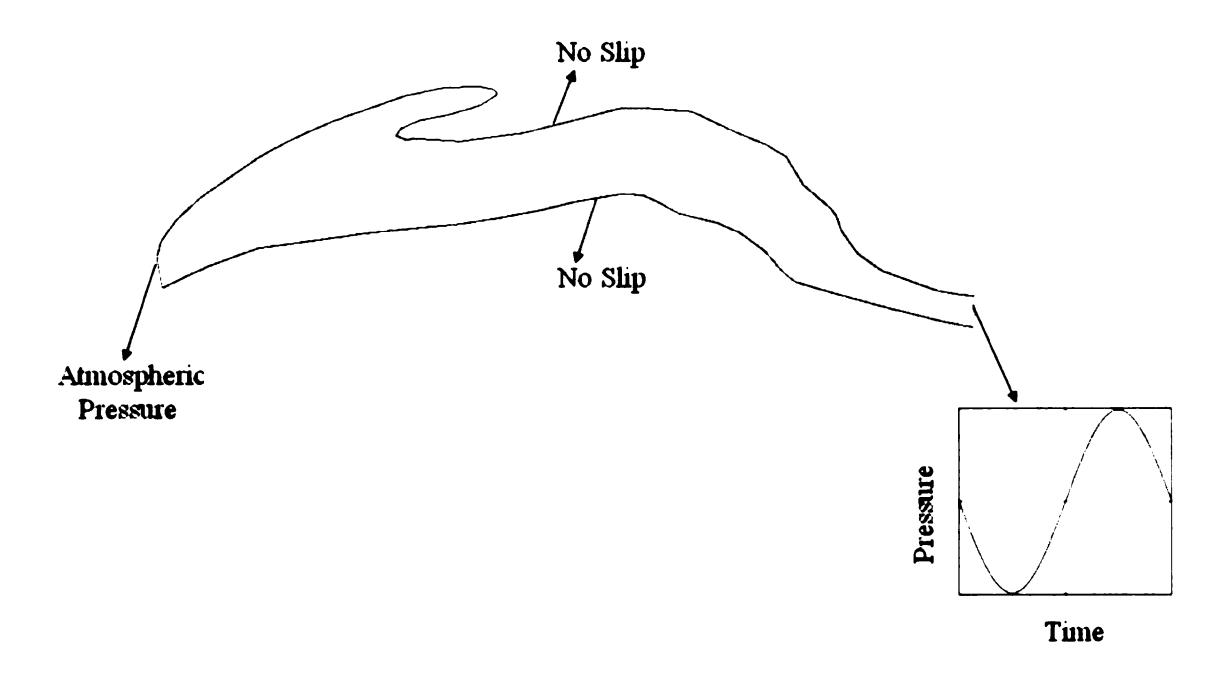


Figure 3.9. Generic boundary conditions for respiratory flow

The frequency and the amplitude of the sinusoidal function applied at the tracheal opening were based on the tracheal pressures and number of breaths per minute for different resting and peak exercising conditions recorded vastly in literature. (e.g., Lumsden et al.). An intermediate state – 'mild exercise' was also introduced. An unsteady pressure function whose amplitude and frequency are about midway between rest and peak exercise was formulated, corresponding to this condition. The sinusoidal unsteady pressure functions applied at the tracheal opening are illustrated in **Figure 3.10** (rest), **Figure 3.11** (mild exercise) and **Figure 3.12** (intense exercise).

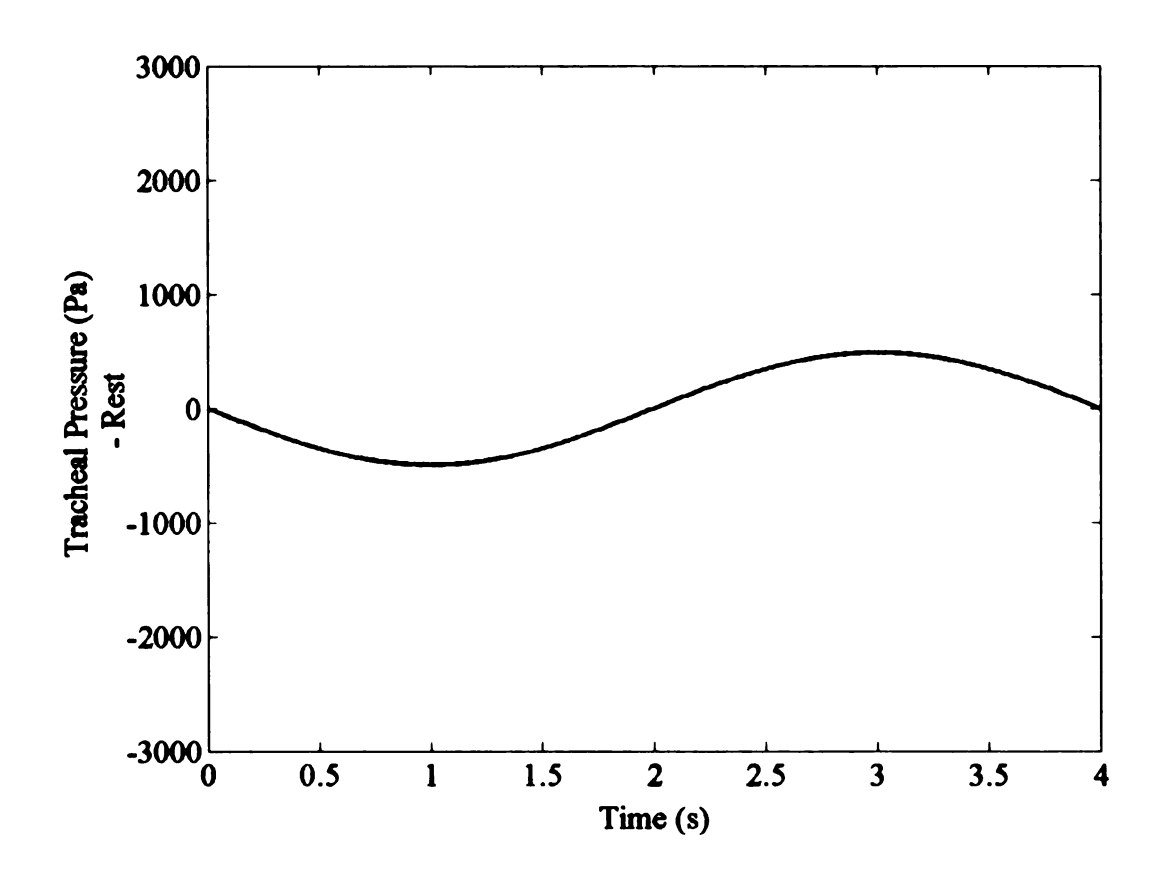


Figure 3.10. Tracheal pressure cycle during rest

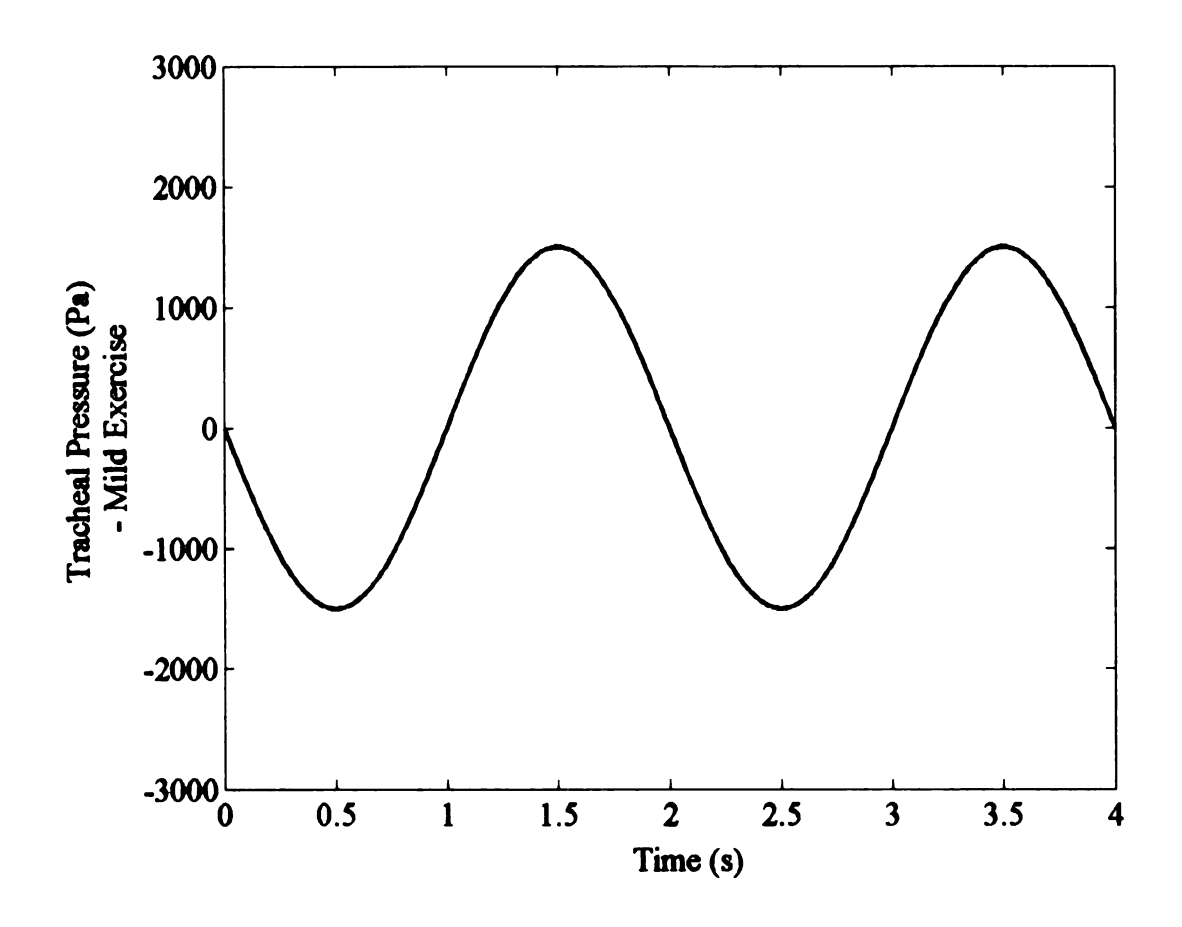


Figure 3.11. Tracheal pressure cycle during mild exercise

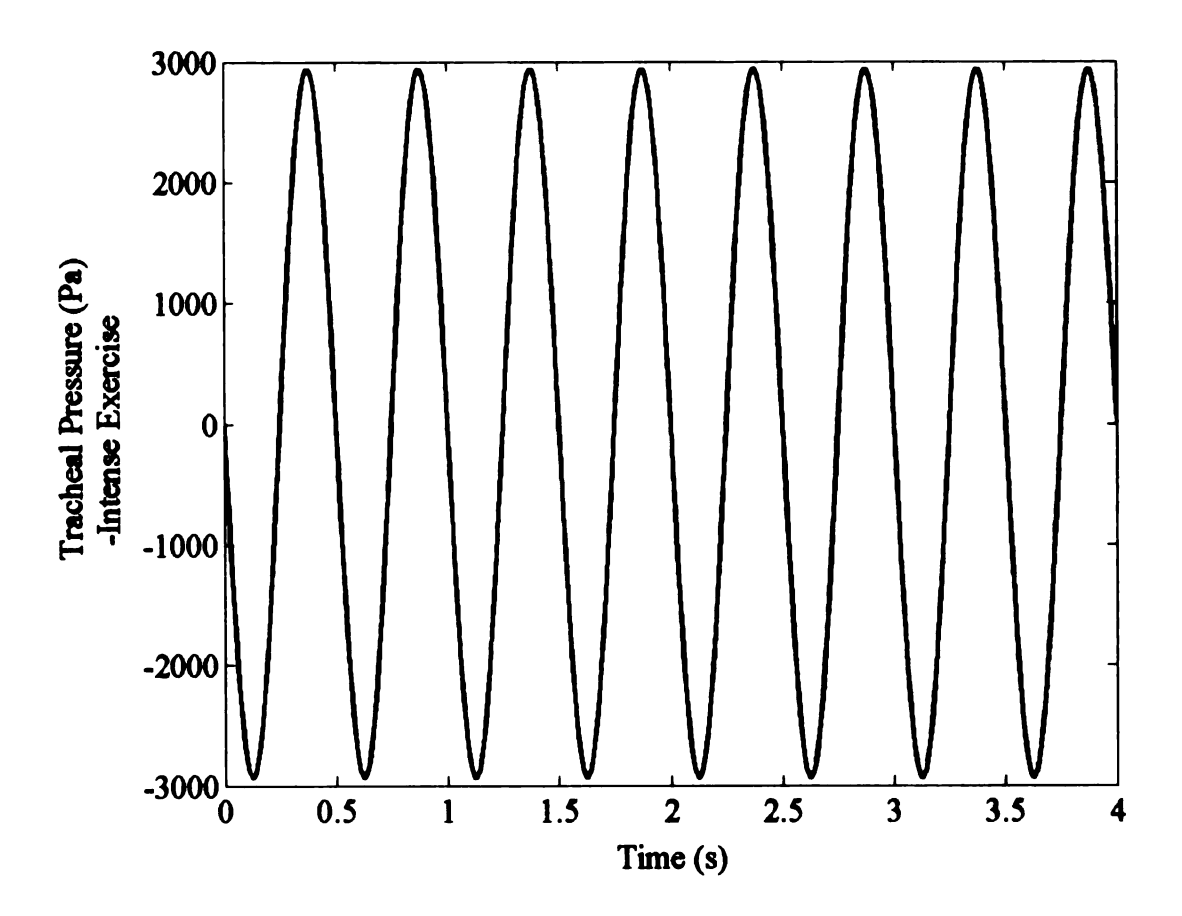


Figure 3.12. Tracheal pressure cycle during intense exercise

As a summary, **Table 3.1** lists the amplitude and the frequency of these time-periodic functions and the breathing rates for the different intensities of exercise.

Table 3.1. Unsteady pressure boundary condition corresponding to different rates of respiration

	Exercise	Maximum Tracheal	Breaths per min.	Frequency
S. No.	Condition	Pressure '   P <sub>max</sub>   ' (Pa)		'f' (Hz)
1.	Rest	490	15	0.25
2.	Mild	1500	60	1
	Exercise			
3.	Intense	2940	120	2
	Exercise			

The tracheal pressure boundary condition was incorporated in such a way that the inhalation half-cycle began first and was followed by the exhalation half-cycle. E.g. for peak exercise, the function applied was:

$$p = -2940\sin\left(4\pi t\right)$$

In order to solve the flow corresponding to the each exercise condition (rest, mild exercise and intense exercise), the corresponding unsteady pressure function was applied. As mentioned earlier, one of the objectives of this study was to study the effects of the artificial flexure introduced into the upper airway on the flow field. Hence, a set of nine numerical computations were performed, each corresponding to a particular degree of artificially induced flexure (none, mild, extreme) and a particular rate of breathing (rest, mild exercise and intense exercise).

The boundary conditions at the top and the bottom walls were standard no-slip wall boundary condition, wherein the fluid velocity at the wall is equal to the velocity of the wall, which in this case equals zero.

Since the energy equation was also solved, it was required to supply appropriate temperature boundary conditions. At the nostril, a standard room temperature of 25 degree centigrade was imposed. At the trachea, temperatures of 30, 35 and 40 degree centigrade were imposed for rest, mild exercise and intense exercise conditions respectively. In order to solve the equations describing the turbulent quantities, it was needed to specify the intensity or turbulence at the inlet and the outlet. This was specified as 1% for resting, 5% for mild exercise and 10% for intense exercise.

#### 3.2.3. Initial condition

Since the flow was initialized to almost no flow throughout the domain (which is an unphysical condition), the solution was monitored for a large number of time steps, covering several time-cycles in order to make sure that the solution attained a time-periodic state. In order to ensure that the time-periodic solution has been achieved, pressures and velocities were monitored at randomly chosen points in the domain and the unsteady state solution was calculated out until time-periodic state was established at all of these points. Once this state was attained, this converged time-periodic solution was saved and that solution was used as a starting point for further simulations. **Figure 3.13** illustrates the location of two points 'a' and 'b 'that were chosen within the domain.

Figure 3.14 shows the variation of pressure with respect to time at point 'a'. And Figure 3.15 shows the variation of the x component of velocity with respect to time at point 'b'. It is seen that these quantities exhibit a time periodic behavior after a few complete cycles.

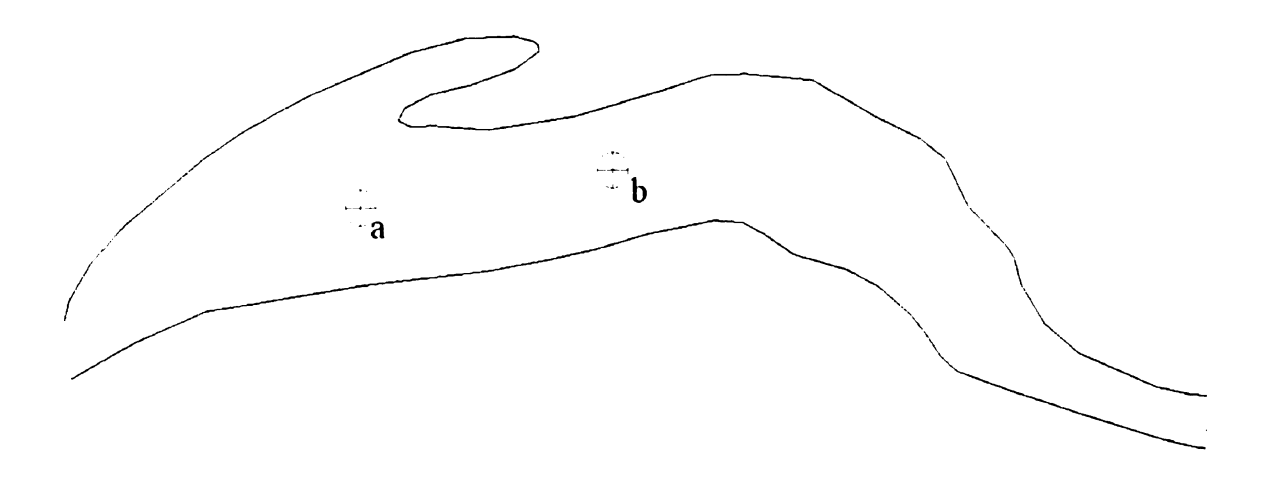


Figure 3.13. Locations of test points within the domain for monitoring solutions

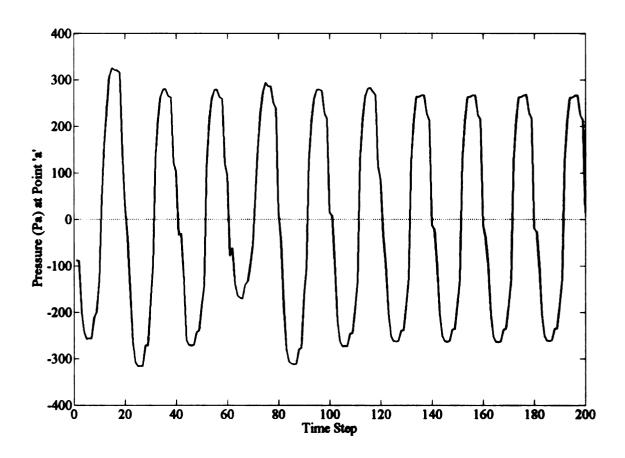


Figure 3.14. Variation of pressure with respect to time at the test point 'a' indicated in Figure 3.13

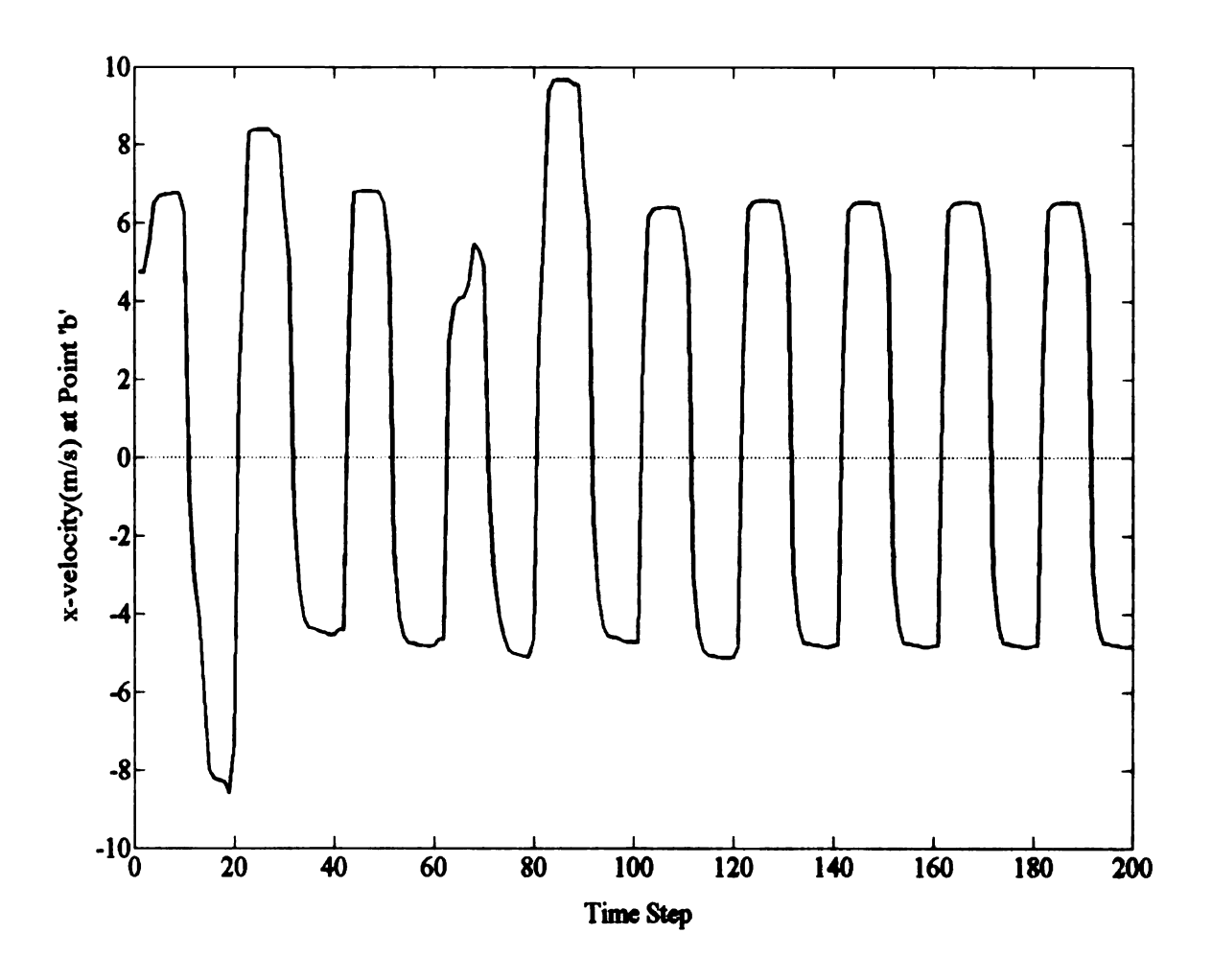
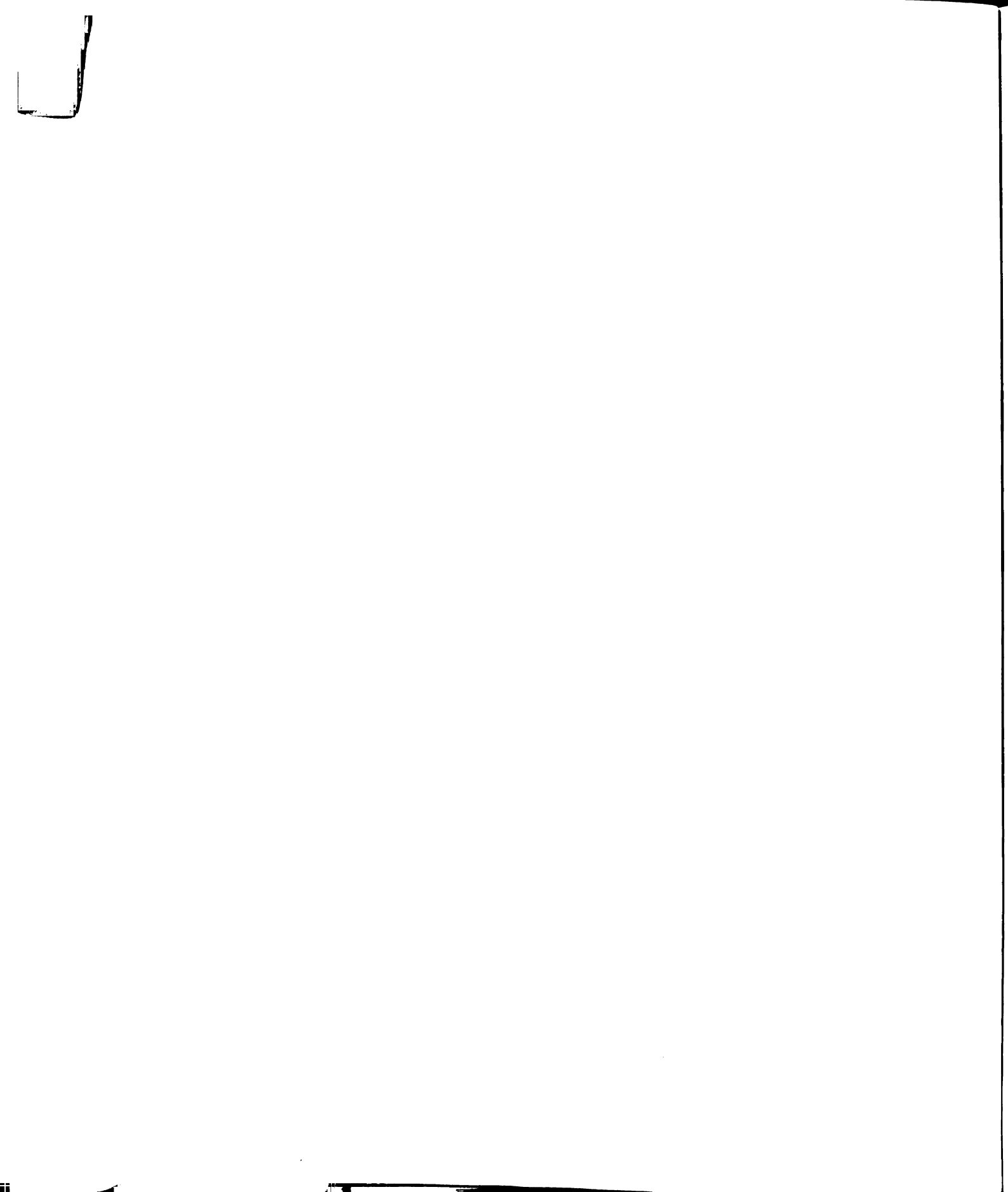


Figure 3.15. Variation of x-velocity with respect to time at the test point 'b' indicated in Figure 3.13

### 3.3. Numerical solution methods

A commercial finite volume based CFD solver (FLUENT 6.2.16, 2 D version) was used to perform the computations. Unsteady, segregated, first-order implicit solver with time steps of 0.025 sec (for exercise), 0.125 (for mild exercise) 0.2 sec (for rest) were used. These time steps were found to be suitable in achieving convergence in a reasonable number of iterations. An unsteady pressure was applied at the outlet, as described earlier. K-epsilon turbulence model was applied and the turbulent quantities were specified by setting the turbulent intensity (1% for rest condition, 5% for mild exercise condition and 10% for intense exercise condition) and hydraulic diameter (0.05 m at the inlet and outlet for all models and respiratory conditions). Convergence of the solution was observed by monitoring the residuals of the five conservation equations. Convergence criteria were set to 1e-3 for the scaled residuals of continuity and momentum equations and 1e-6 for those of k, e and energy equations. First order upwind scheme was used for the convective terms.

For each case, in order to compute the solution over one complete breathing cycle, it took about 3 hours on a Pentium 4, 2.4 GHz CPU. The solution was computed for 10 complete breathing cycles, starting with zero velocity initial condition at all nodes, in order to achieve a time-periodic state. The solution at the end of 10 complete breathing cycles was used as an initial condition for computations from that point onwards. Once a time-periodic state was achieved, the computations were performed for one complete breathing cycle and the solutions at each time step was recorded in the form of a data file.



#### 3.4. Choice of turbulence model

This section describes the reasoning behind the choice of the k-epsilon turbulence model for this problem.

In order to close the Reynolds stress term introduced by the averaging operator applied in the RANS equations, various models have been developed. The k-ε and k-ω are models belong to the broader class of 'two-equation models', which are based on the turbulent viscosity hypothesis. Yet another model, known as the Reynolds Stress Model has been developed in order to provide closure to the RANS equations. This model is widely regarded as very appropriate when resolving the boundary layers, near wall regions are important and when the mainstream velocity exhibits appreciable variation over macroscopic time-scales. For this reason, Reynolds Stress Model would be the most appropriate choice for this problem. However, the computational effort required is significantly large in this case because of the additional equations introduced, each corresponding to a particular component of the Reynolds stress (presenting these equations here is beyond the scope of this work). For the sake of a benchmark comparison, the flow was solved for mild exercising conditions for the mild induced flexure geometry using RSM, k-epsilon and k-omega models. The solutions were compared by observing the velocity profiles established at different cross-sections throughout the domain. Figure 3.16 shows two such cross sections – A1-A2 and B1-B2 that were chosen to compare the velocity profiles established using each of the turbulence models mentioned above. Figure 3.17 is a plot of the velocity profiles across cross section B1-B2.

From such comparisons, it was observed that there was no significant difference in the average velocity across the cross-section between the k-epsilon and the RSM models, whereas the k-omega model differed slightly. Due to greater ease of use and greater efficiency in achieving convergence faster, the k-epsilon model was used to model turbulence in this problem.

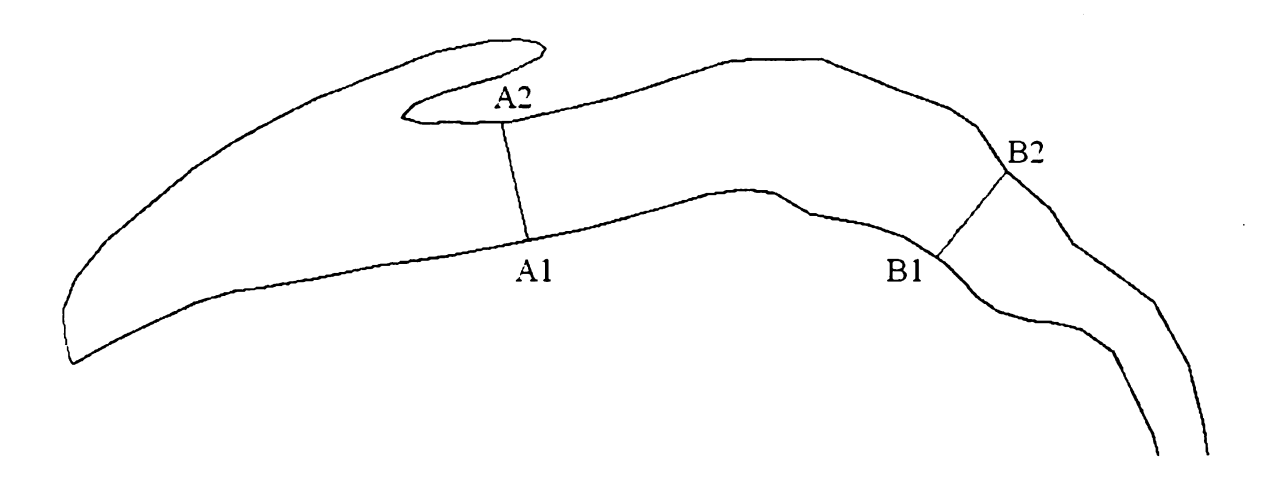


Figure 3.16. Locations of test surfaces within the computational domain for comparing solutions obtained using different models

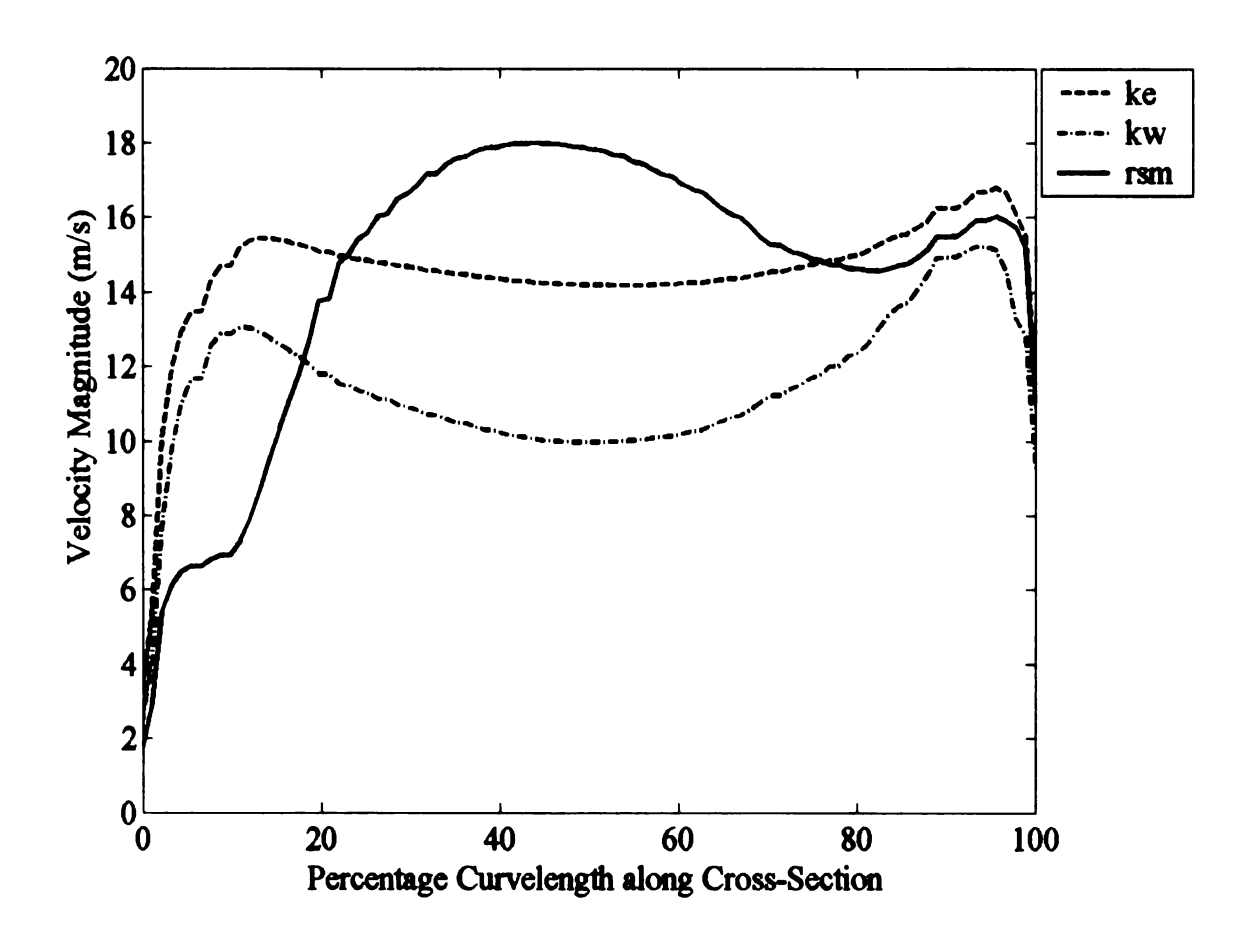


Figure 3.17. Comparison between k-epsilon, k-omega and RSM model based solutions – velocity profile at cross-section B1-B2

A similar comparison across section A1-A2 yielded similar inferences.

# 3.5. Assumptions in modeling

The following are the important assumptions of this work:

- The model that was developed from a dead horse adequately represents all the features of the living horse, especially with respect to collapsible tissues like nostrils.
- Variation of flow parameters in the z direction (indicated in Figure 3.18) is negligible.

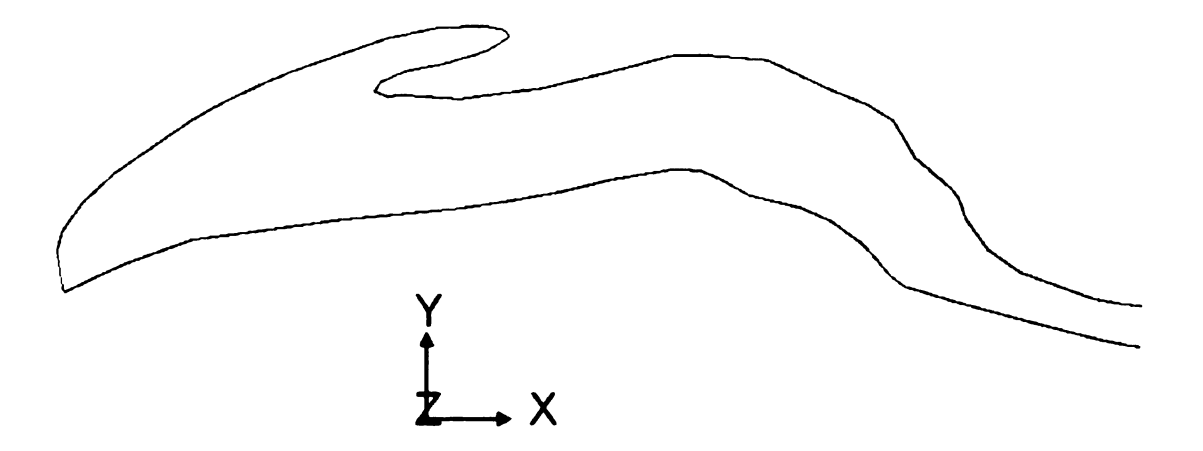


Figure 3.18. Orientation of the coordinate axes within the domain

- The models corresponding to the different degrees of flexure closely correspond to the flexure induced by pulling the reins.
- The model is closely comparable to horses of different sub-species and genders.
- The flow is single phase. i.e., the effects of moisture during exhalation half-cycle are not important.
- The tracheal pressure is a time periodic function given by a sinusoidal function of time.

- The dynamic changes in geometry due to the horse's gait and gallop are negligible.
- The dynamic changes in the geometry due to collapse of tissues such as soft palate, nostril etc. into the airway are negligible.
- The air entering the horse's nostril has zero velocity, i.e. the effect of air entering the nostrils with a certain speed when the horse is racing or due to environmental factors like wind etc. are not important.
- Inspired and expire air have same properties. i.e., Changes in properties like specific heat, density etc., are negligible.
- The weight of the jockey riding the horse has negligible effect in the driving pressures in the trachea.
- The walls of the model are rigid. While in reality, the tissues that make up the wall of the domain are pliant and change the cross sectional areas throughout the breathing cycle.

# **CHAPTER 4: RESULTS AND DISCUSSION**

Validation details, results and discussions are presented in this chapter.

### 4.1. Validation

Experimental (recorded in Lumsden et. al [16]) and numerically calculated values of flow rates at peak inspiration and at peak expiration were compared. The comparison is shown in **Table 4.1**.

Table 4.1. Comparison between experimental and numerical results

Exercise condition	Peak inspiratory flow rate (L/s) - (experimental)	Peak expiratory flow rate (L/s) - (numerical)
Rest	3.50	5.92
Mild exercise	42.98	46.92
Peak exercise	78.21	81.00

The experimental values presented in the table are interpolated values from the actual experimental values. The interpolation was done in order to match the flow rates with the exact breathing frequencies corresponding to which the numerical calculations were performed.

From the unsteady state computation, the time steps corresponding to peak inspiration and peak expiration were noted. At these time instants, flow rates across the nostril inlet boundary were calculated. The two-dimensional numerical solutions delivered the flow rates based on a unit channel width, which in this case equals one meter. These values were scaled down to an equivalent channel width for the nostril opening corresponding to rest (1 cm), mild exercise (3 cm) and intense exercise (6 cm) in order to account for the expansion of the nostrils during exercise. Numerically calculated values for peak flow rates were found to be comparable with experimental values.

# 4.2. Velocity and pressure distributions:

It is worthwhile to study the velocity and pressure distribution throughout the domain at important time instants in an unsteady state solution in order to be able understand the solution. Hence, the pressure contours and mean velocity vectors were drawn at the time instants corresponding to the occurrences of peak inhalation, end of inspiration and beginning of expiration, peak expiration and end of expiration and beginning of inspiration. These were the time instants at which unique patterns of distributions of velocity and pressure were expected. In order to know the exact time steps at which these events occurred, the velocity vector distributions were studied from the solutions at each time step from the start to the end of the respiratory cycle. For instance, the instant when the maximum magnitudes of velocities were observed at the inlet in the inspiratory flow direction was considered as the instant corresponding to 'peak inspiration'.

# 4.2.1 Velocity and Pressure distributions through the tracheal pressure cycle

Figure 4.1 shows the velocity field during peak inspiration and during intense exercise for a non-flexed model. The velocity vectors are colored and scaled according to their magnitudes. The graph in Figure 4.2 indicates the portion of the tracheal pressure cycle that is completed at the instant when peak inspiration occurs. The beginning of the tracheal pressure cycle is considered here as the instant at which the pressure at the trachea is zero and is about to become negative, as dictated by the boundary condition that was supplied. The shaded area in the Figure represents the part of the tracheal pressure cycle completed just when peak inspiration occurs.



Figure 4.1. Velocity distribution (m/s) at peak inspiration

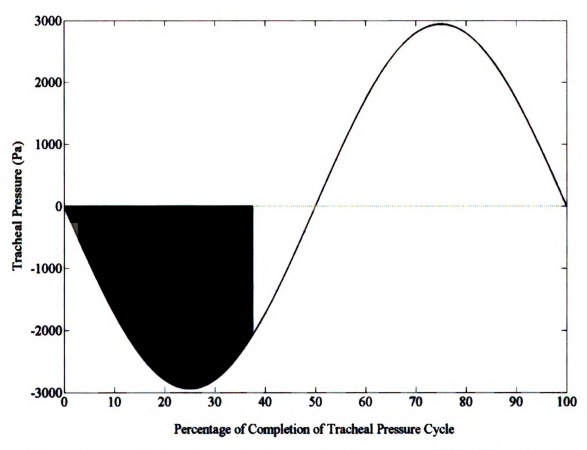


Figure 4.2. Occurrence of peak inspiration relative to the tracheal pressure cycle

The peak velocities were observed near the inlet and the outlet (viz., the nostril and the tracheal opening). Although one would expect the peak velocities (and hence peak inspiratory flow) to occur at a time instant when the driving pressure is maximum, this was not what was observed. The tracheal pressure is at its negative peak at the time instant corresponding to the completion of 25% of the tracheal pressure cycle. After this instant, the pressure decreases in magnitude, while still remaining negative until 50% of the cycle is completed. From **Figure 4.2**, it can be seen that the peak inspiration occurred when 40% of the tracheal pressure cycle is completed, when the driving pressure is lower than that at 25% completion of pressure cycle. This lag between the expected occurrence of peak inspiration and the actual occurrence of peak inspiration indicates that the effect of compressibility of the fluid elements is pronounced in time-periodic oscillatory flows, especially at higher pulsating frequencies. If the fluid elements were totally incompressible, then a pressure change at the end of the airway should be 'sensed' instantly by the fluid elements, thus making the velocities in phase with the pressure.

Yet another interesting observation was that the streamlines followed a curved path during inspiration in order to maneuver around the swirl created near the nostril area due to the presence of the turbinates where almost zero velocity was observed. The flow through the remaining part of the nasal cavity and the nasopharyngeal region was observed to be devoid of any eddies. **Figure 4.3** shows the pressure contours during the same time instant (peak inspiration). An important observation from this figure is that the pressure in the pharynx and the mid-nasal cavity is fairly constant at -1000 Pa (gauge) and about -2000 Pa at certain pockets around the soft palate and the pharynx.



Figure 4.3. Pressure contours (Pa) at peak inspiration

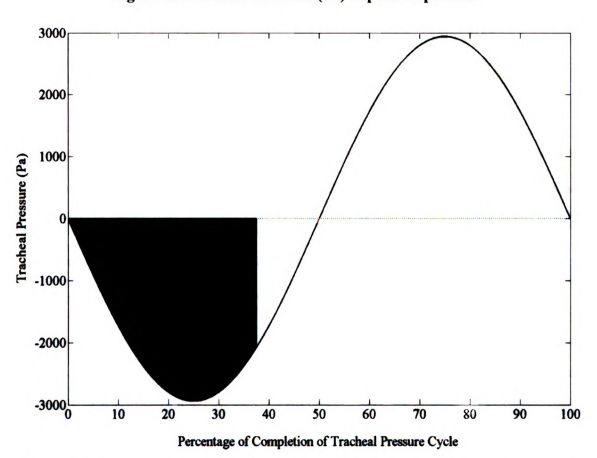


Figure 4.4. Occurrence of peak inspiration relative to the tracheal pressure cycle

Figure 4.5 shows the velocity distribution during the end of the inspiration half-cycle and just at the beginning of the expiratory half-cycle. At this instant, the fluid elements are about to reverse their directions and go from the trachea to the nostril due to positive gauge pressure at the trachea. In Figure 4.6, the occurrence of the end of inspiration relative to the tracheal pressure cycle is shown. However, as is evident from the Figure, all the fluid elements do not reverse their directions simultaneously. From observing the figure, it can be hypothesized that the fluid elements near the trachea start 'sense' the change in tracheal pressure from negative to positive gauge earlier than those fluid elements near the nostril. Hence, the fluid elements near the pharynx and the tracheal opening start following an expiratory flow direction whereas those fluid elements near the nostril still follow an inspiratory flow direction. As a result, swirls are formed due to the mixing of a set of fluid elements moving in one direction with those moving in the opposite direction.

Due the lag effect due to compressibility, as discussed earlier, flow reversal from inspiration to expiration does not occur at the instant at which zero pressure difference occurs between the nostril and the trachea (which is at 50% of completion of the tracheal pressure cycle). Instead, this occurs at about 60% into the pressure cycle which is way past the instant at which the tracheal pressure becomes zero from negative gauge.

Figure 4.7 shows the pressure contours at end of inspiration and beginning of expiration and Figure 4.8 indicates the occurrence of this even relative to tracheal pressure cycle. Variation in pressure from the nasal cavity to the tracheal opening appears to be gradual.

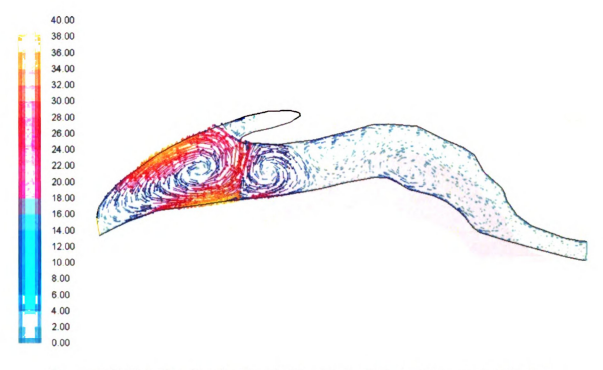


Figure 4.5. Velocity distribution (m/s) at end of inspiration and just before expiration

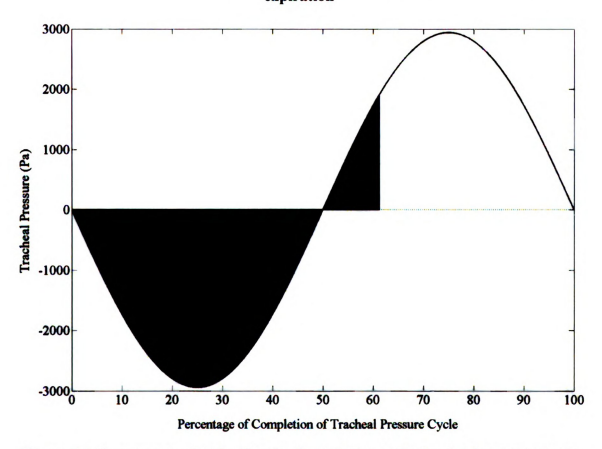


Figure 4.6. Occurrence of end of inspiration relative to the tracheal pressure cycle



Figure 4.7. Pressure contours (Pa) at end of inspiration and just before expiration

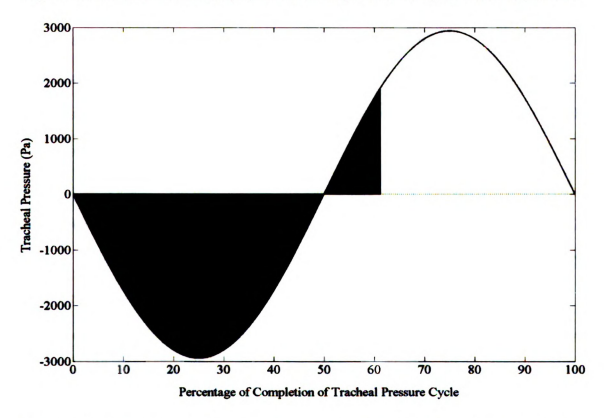


Figure 4.8. Occurrence of end of inspiration relative to the tracheal pressure cycle

Figure 4.9 shows the distribution of velocity distribution during peak inspiration and Figure 4.10 and show the time instant in the tracheal pressure cycle during which this event occurs. Here again, the lag between the expected occurrence and the actual occurrence of the event is observed. The maximal expiratory driving pressure would occur at the instant of 75% completion of the tracheal pressure cycle. Hence peak expiration is found to occur at this time instant. Instead, peak expiration is found to occur at about 90% completion of the unsteady pressure cycle, when the driving pressure is much lower compared to that at 75% completion. The streamlines near the nostril take a dorsal (towards the horse's backbone) curved path before exit as opposed to the ventral (towards the horse's belly) curved path taken by the streamlines during peak inspiration. The fluid elements appear to take this path because of negotiating a swirl established in the nasal cavity as seen in Figure 4.9. At this instant, peak velocities were observed near the inlet and the outlet (viz. the tracheal opening and the nostril). At the pharynx and the inner nasal cavity, velocity magnitudes are smaller and vary more gradually. This could be attributed to the increase in cross-sectional area as a fluid element moves from the trachea to the pharynx during expiration.

Figure 4.11 describes the pressure contours during peak expiration and Figure 4.12 indicates the occurrence of peak expiration relative to the tracheal pressure cycle. The maximum pressure occurs at the pharyngeal cavity which is at about 1700 Pa (gauge). It is to be noted that this pressure is higher than the driving pressure at the tracheal opening which is at about 1200 Pa (gauge).

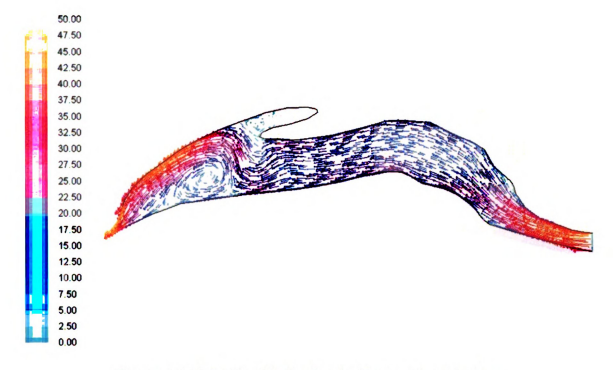


Figure 4.9. Velocity distribution (m/s) at peak expiration

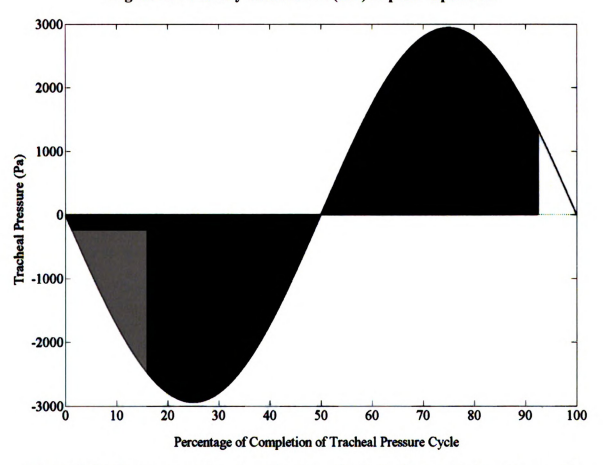


Figure 4.10. Occurrence of peak expiration relative to the tracheal pressure cycle



Figure 4.11. Pressure contours (Pa) at peak expiration

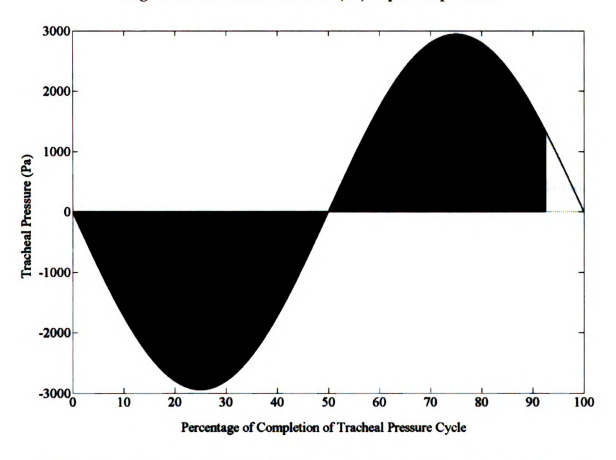


Figure 4.12. Occurrence of peak expiration relative to the tracheal pressure cycle

Figure 4.13 shows the velocity distribution at the end of the expiration-cycle and at the beginning of the inspiration-cycle. Figure 4.14 shows the percentage of the tracheal pressure cycle completed when this event occurs. The flow reverses from exhalation to inhalation at this instant. Most of the domain has close to zero velocity, except near the nostril and at the pharynx where there are swirls with velocities ranging from 0 to 16 m/s. Both of these regions have a geometric similarity – both of them involve rapid expansion in area. The swirl that is seen at the pharynx is just above the epiglottis muscle. The velocity in the vicinity of the posterior region of the soft palate and the epiglottis appears to be greater than the surrounding regions due to the effect of the swirl.

Here again, due to inertial effects there is a lag between the time instant at which this event is to occur and the time instant at which this actually occurs. Rather than at the start of the tracheal pressure cycle, beginning of inspiration occurs at about 8% into the tracheal pressure cycle.

Figure 4.15 shows the pressure contours at end of expiration and beginning of inhalation and Figure 4.16 indicates the portion of the tracheal pressure cycle completed when this event occurs. The pressure distribution varies gradually from 100 Pa at the nostril end and about -1600 Pa at the tracheal end, as indicated by the striations in the contours along the upper airway.

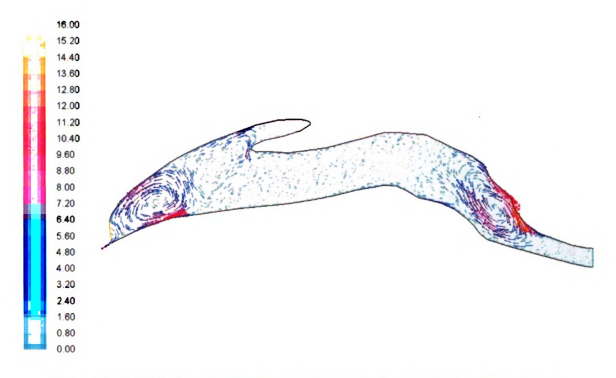


Figure 4.13. Velocity distribution (m/s) at end of expiration and just before inspiration

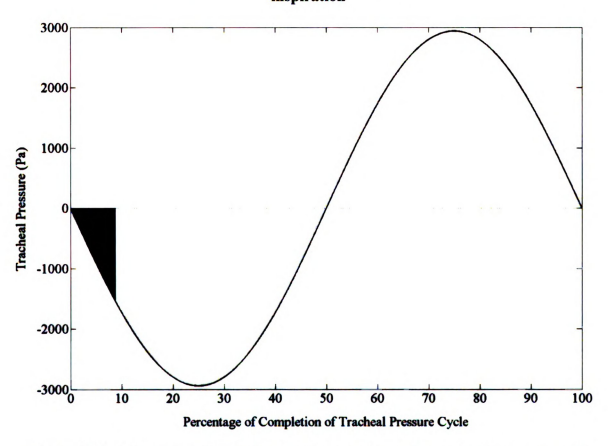


Figure 4.14. Occurrence of end of expiration relative to the tracheal pressure cycle



Figure 4.15. Pressure contours (Pa) at end of expiration and just before inspiration

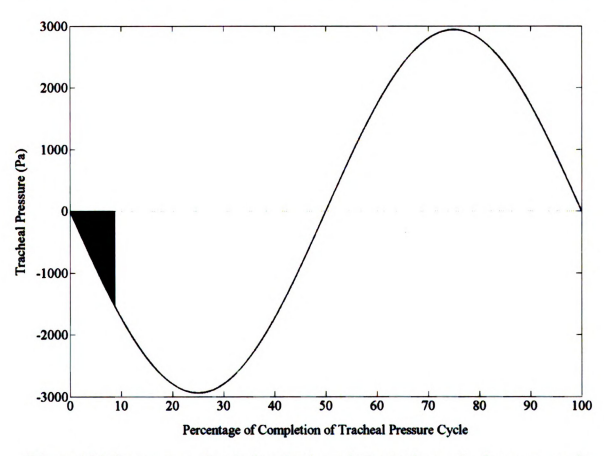


Figure 4.16. Occurrence of end of expiration relative to the tracheal pressure cycle

#### 4.2.1. Variation in velocity distribution with respiratory rate

The flow field in this problem is dependent upon two broad parameters: Rate of respiration and degree of artificially induced flexure. In order to study the sensitivity of the solution to the rate of respiration alone, the velocity distribution given by solutions corresponding to rest, mild exercise and intense exercise for a given degree of induced flexure and at different time instants were plotted and studied. Such velocity vector plots for no induced flexure model and at end of inspiration are shown in this section. In section 4.2 it was observed that the time instant corresponding to the end of inspiration and beginning of expiration had the strongest swirls. Hence, this time instant was chosen to compare solutions corresponding to the different breathing rates.

Figure 4.17, Figure 4.18 and Figure 4.19 show the velocity distribution corresponding to rest, mild exercise and intense exercise respectively at end of inspiration (beginning of expiration) for the non flexed geometry. Each of these Figures has been plotted to a common scale so that they can be compared with ease.

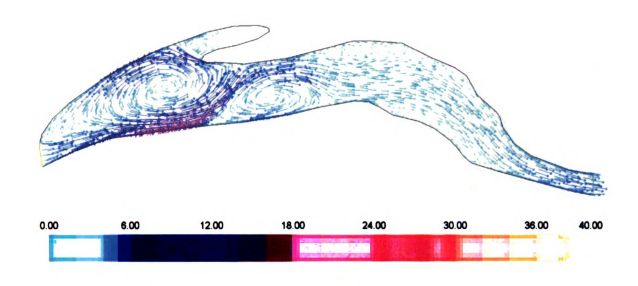


Figure 4.17. Velocity distribution (m/s) at end of inspiration - rest condition

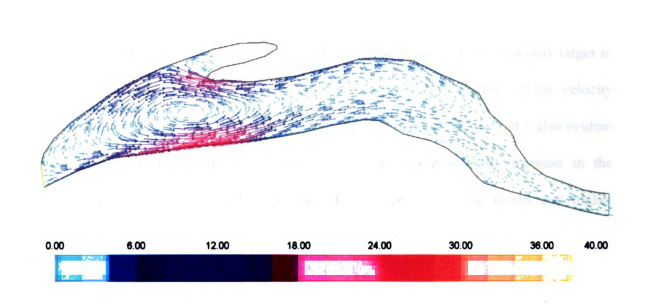


Figure 4.18. Velocity distribution (m/s) at end of inspiration - mild exercise condition

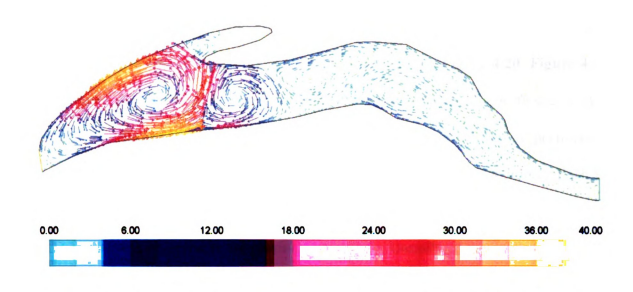


Figure 4.19. Velocity distribution (m/s) at end of inspiration - intense exercise condition

From the above comparisons, one can observe that at rest, the swirl formed in the anterior nasal cavity has velocities ranging from 0-18 m/s. Whereas, during mild and intense exercise conditions, the swirl(s) in the vicinity of the soft palate is (are) not only larger in terms of physical dimensions, but are also more significant in terms of the velocity gradients (0-30 m/s for mild exercise and 0-40 m/s for intense exercise). It's also evident from this comparison that the velocity at any point increases with increase in the respiration rate, which is quite obviously due to greater driving forces and higher frequencies.

#### 4.2.2. Variation of velocity distribution with flexure in upper airway

In order to study the sensitivity of the solution to the degree of induced flexure alone, the velocity distribution given by solutions corresponding to non-flexed, mildly flexed and extremely flexed geometries for a given rate of respiration at different time instants are plotted and studied. These velocity plots during intense exercise and at the instant corresponding to end of inspiration are shown in this section. Figure 4.20, Figure 4.21 and Figure 4.22 show the velocity distribution corresponding to non-flexed model, model with mild induced flexure and model with extreme induced flexure respectively at end of inspiration (beginning of expiration) for intense exercising condition. Each of these Figures has been plotted to a common scale so that they can be compared with ease. Unlike what was observed in the previous section, the intensity of the swirls, in terms of velocity range was not found to vary significantly in a definite way between non-flexed, mildly flexed and extremely flexed geometries. This might indicate that the solution is more sensitive to the rate of respiration than it is to the degree of induced flexure.

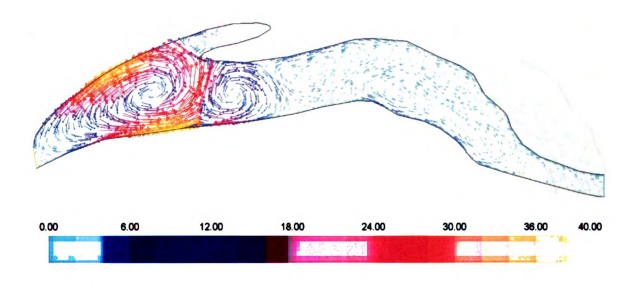


Figure 4.20. Velocity distribution (m/s) at end of inspiration - no induced flexure

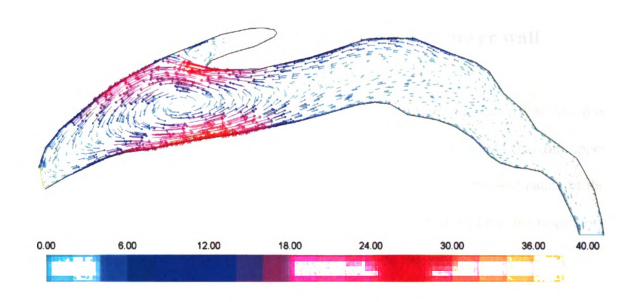


Figure 4.21. Velocity distribution (m/s) at end of inspiration - mild induced flexure

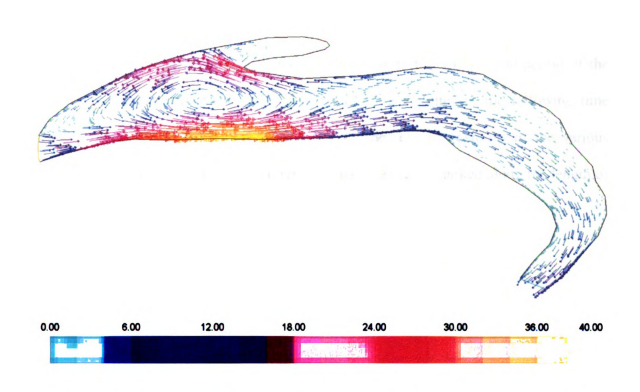


Figure 4.22. Velocity distribution (m/s) at end of inspiration – extreme induced flexure

# 4.3. Wall pressure along the dorsal surface of lower wall

As mentioned in chapter 1, in a horse with the DDSP condition, the soft palate which is usually held in position by the epiglottis muscles is displaced upwards into the upper airway. Hence, it expected that there will be a net upward force on the soft palate of the lower wall of the geometry in general, at least during brief periods of time in a respiratory cycle. In order to understand if there is a lift created on the lower wall of the geometry and to know the time instants at which this situation occurs, wall pressures along the lower wall were plotted from the nostril end to the tracheal end at different time instants. One such plot is shown in **Figure 4.23** where the wall pressures from the solution corresponding to extremely flexed geometry under intense exercise condition are plotted at different time instants throughout the breathing cycle. If T is the time period of the tracheal pressure function, the lower wall pressures are plotted at the following time instants: when t = T, 0.1 T, 0.5 T, and 0.6 T. The relative positions of the various anatomical features relevant to the current discussion are also marked along the length of the lower wall.

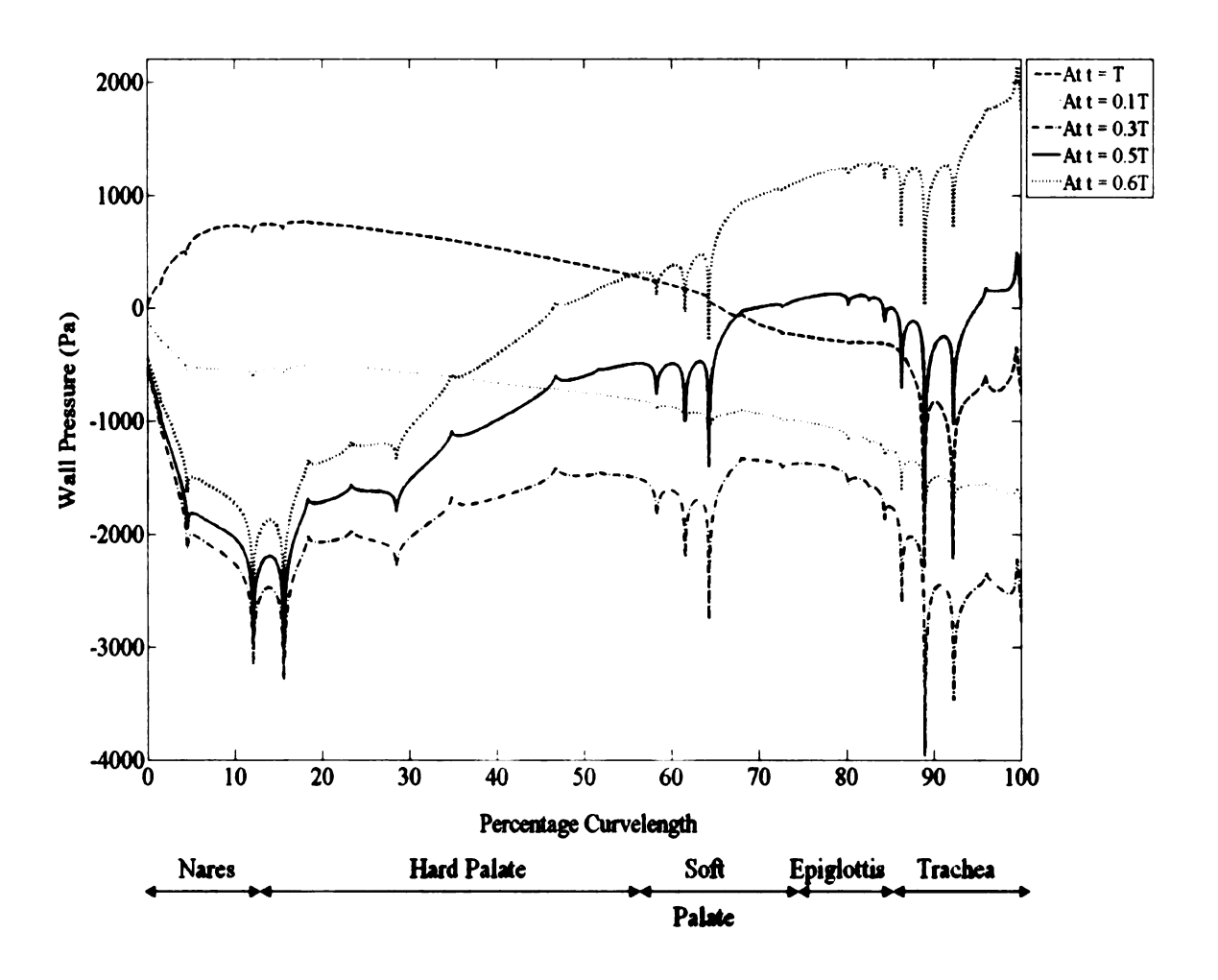


Figure 4.23. Wall pressure along dorsal surface - variation through the tracheal pressure cycle

From the above Figure, it can be observed that the lowest pressure along the bottom wall occurred when at about 30% of completion of the pressure cycle. At this instant, the flow was observed to be close to peak inspiration (from section 4.1). The pressure at the dorsal surface of the bottom wall exhibited time-periodic variation. Near the nostril at time instants between 0.3 T and 0.6 T, high gradients of wall pressure were observed. This could be due to the entrance effects contributing to increased turbulence when the flow rates are close to being peak inspiratory flow rates. Over the most of the hard palate, the wall pressure was observed to remain either near-constant or vary gradually, except at the

end connecting to the soft palate. In that region and the one that continues further into about 30% of the soft palate, high wall pressure gradients were observed. This could be attributed to the rapid change in the cross-sectional area and also due to the flexure in the geometry (even the non-flexed model has a mild natural flexure) resulting in curvature of the streamlines and hence in the formation of eddies contributing to greater turbulence. High magnitudes of wall pressure gradients were found to occur at the portion of the trachea connecting to the epiglottis as well.

In general, lower pressures were found to occur at times close to those corresponding to the peak inspiration times (0.3 T). At this time instant, pressures were found to reach up to maximum negative values of -3000 Pa in regions adjacent to the soft palate and the nostrils, and up to -4000 Pa in the regions near the epiglottis-tracheal interface. For these times, the wall pressure gradients were also found to be greater.

## 4.3.1. Variation of wall pressure distribution with respiratory rate

To understand the effect of the rate of respiration on the lift created on the lower wall and the soft palate in particular, the lower wall pressures at time instant t = 0.3 T were plotted (**Figure 4.24**) from the solutions corresponding to non-flexed geometry for rest, mild exercise and intense exercise conditions. The time instant corresponding to t = 0.3 T was chosen because from the earlier section, it was observed that the least wall pressures occurred at this time step.

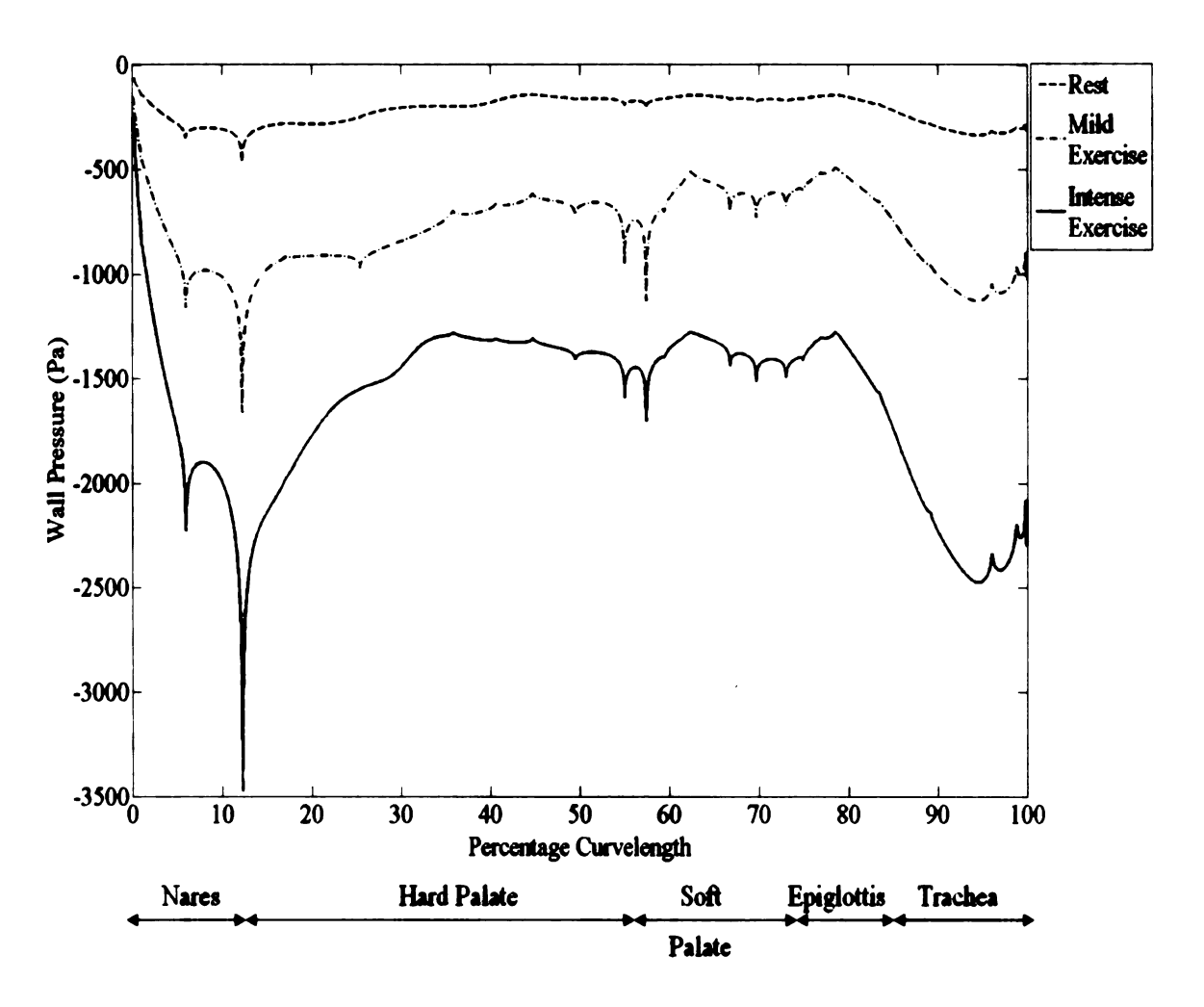


Figure 4.24. Wall pressure along dorsal surface - variation with rate of respiration

It can be inferred from Figure 4.24 that for a given flexure, the wall pressure during peak inspiration decreases with intensity of respiration. Moreover, wall pressure gradients are also found to be more pronounced at intense exercise conditions. This might explain could possibly explain why DDSP should, quite often, manifest only during intense exercise.

# 4.3.2. Variation of wall pressure distribution with induced flexure in the upper airway

To understand the effect of artificially induced flexure on the lift created on the lower wall and the soft palate in particular, the lower wall pressures at time instant t = 0.3 T were plotted (**Figure 4.25**) from the solutions corresponding to intense exercise condition for the non-flexed and the extremely flexed models. Here again, the time instant corresponding to t = 0.3 T was chosen because from the section 4.2, it was observed that the least wall pressures occurred at this time step.

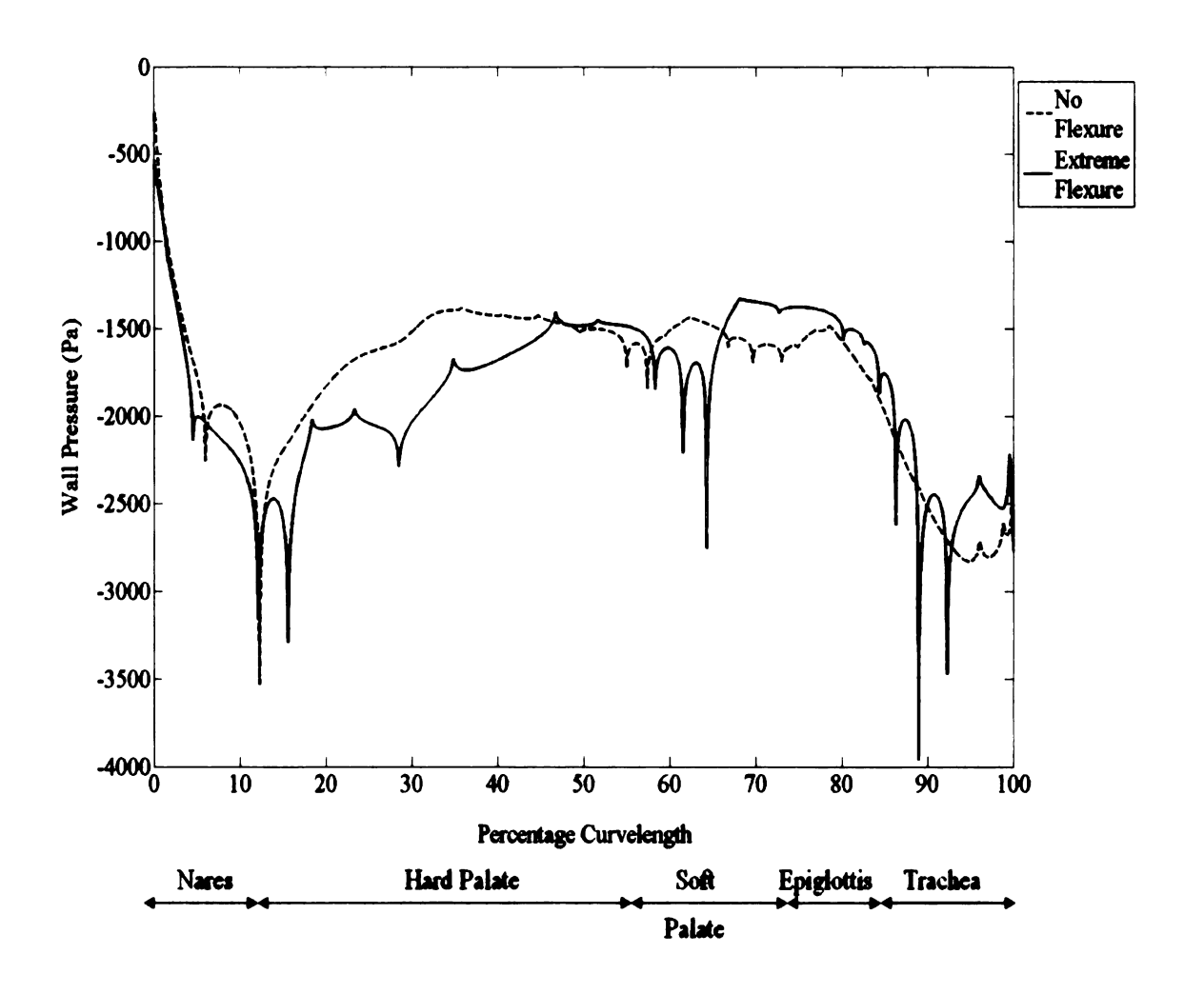


Figure 4.25. Wall pressure along dorsal surface – variation with induced flexure

Figure 4.25 clearly shows that with a greater flexure in the airway, the pressure gradients along the wall, especially around the soft palate and the epiglottis are greater. This could be attributed to the additional curvature of the streamlines. The soft palate region, the epiglottis region and the entrance to the trachea region of the lower are observed to have high pressure gradients (gradients of wall pressure along the surface of the lower wall).

# **CHAPTER 5: CONCLUSIONS AND FUTURE WORK**

The equations governing the respiratory flow of air within the equine upper airway were solved numerically. Solutions were obtained for airflow under different rates of respiration viz. rest, mild exercise and intense exercise and corresponding to different airway geometries viz. non-flexed, mildly flexed and extremely flexed. Each of these solutions was analyzed by plotting the velocity and pressure distributions at various time instants throughout the respiratory cycle. The pattern of airflow established was found to be uniquely determined by the upper airway geometry and by the rate of respiration.

At peak inspiration during intense exercise, the pressures in the pharynx, the posterior and mid-nasal cavity were fairly constant at a value of -1000 Pa with pockets of even lower pressures reaching up to about -2000 Pa at certain regions along the dorsal surface of the lower wall that are adjacent to the soft palate, the epiglottis and anterior pharynx. Wall pressures along the dorsal surface of the lower wall were found to reach up to maximum negative values of -3000 Pa adjacent to the soft palate and the nostrils, and up to -4000 Pa near the epiglottis-tracheal interface. The lift forces set up on the lower wall due of these highly negative wall pressures and luminal pressures could reach such high values that might not be balanced by the downward forces applied on the pliant structures like soft palate by the restraining muscles of the upper airway. Hence the soft palate and other such pliant tissues of the upper airway may have a natural tendency to get displaced into the airway.

In addition to being subjected to highly negative wall pressures and luminal pressures, the regions along the dorsal wall adjacent to the soft palate and the epiglottis-tracheal interface are also subjected to high wall pressure-gradients. These sharp variations in wall pressure may be instrumental in destabilizing the muscles of the soft palate and/or the epiglottis, facilitating the dorsal displacement of the soft palate.

The velocity plots drawn at various instants through the respiratory cycle indicate that in the nostril, the anterior nasal cavity and the posterior pharyngeal cavity, the flow is complex with swirls observed frequently. The intensity of these swirls in terms of ranges of velocity magnitudes increase with increase in respiration rate and driving pressures. Since increase in swirling motion is often linked with increase in the intensity of turbulence, it is possible that the increased magnitudes of fluctuating components of velocities during intense exercise may be inducing to the soft palate muscles, an unsteady fluttering motion, or a tendency to flutter, thereby contributing to dorsal displacement of soft palate.

The phenomena mentioned above viz. swirling flows in the posterior pharyngeal cavity and highly negative dorsal wall pressures and dorsal wall pressure-gradients adjacent to the soft palate-epiglottis region were observed to be more pronounced under conditions of intense exercise. This might explain why the condition of DDSP is not diagnosable in horses at rest. Similarly, the highly negative dorsal wall pressures and dorsal wall pressure-gradients adjacent to the soft palate-epiglottis region were more pronounced with increase in degree of induced flexure in the upper airway. This might explain why

the condition of DDSP is at times not diagnosable through tests at high speeds on a treadmill in a horse with a history of the condition while racing, since this testing situation is not representative of an actual racing situation where there is a flexure introduced in the airway. This may also explain why this condition in many cases is manifested almost exclusively while racing as under this situation, not only do rapid breathing rates prevail, but also an additional flexure to the airway is introduced by the pulling of the reins.

It is possible that the condition of DDSP is initiated by strong negative pressures along the dorsal surface of the soft palate and that the displacement of the soft palate into the airway causes a reduction in the cross-sectional area of the upper airway which in turn decreases the pressure inside the airway in the vicinity of the soft palate, facilitating a dynamic collapse of the soft palate into the airway. Whether DDSP will occur or not, given a prevalence of large negative dorsal wall pressures along the soft palate would depend on other factors like – stiffness of the soft palate and its holding muscles including the epiglottis (which in turn may be influenced by other factors including the age of the horse), existence of other upper airway respiratory disorders such a pharyngeal collapse, existence of certain neuromuscular disorders, etc.

From this study, it is possible to conclude that the pattern of airflow established is at least partly responsible for the dorsal displacement of soft palate. Intense exercise and high degree flexure in the upper airway may be favorable factors for DDSP to occur. A

qualitative estimate of the individual contribution of these factors in causing DDSP was beyond the scope of this study.

Our analysis assumed the flow to be varying only along the plane, defined by the sagittal section of the geometry. A three dimensional representative geometry would provide better insights into the flow simulations. The soft palate portion of the lower wall could be modeled to represent a pliant tissue instead of a rigid wall. This might help one visualize the occurrence of DDSP. For the sake of simplicity, a sinusoidal function of time was applied to describe the unsteady pressure boundary condition at the tracheal boundary. An analytical function of time, constructed from curve-fitting time history data of the actual outlet pressure values recorded from experiments, to describe the variation in the driving pressure. It might be worthwhile to study the effects of the entry conditions of the air entering the nostril on the distribution of pressure and velocity throughout the domain. That study might throw light on the dependence of DDSP on the racing speed and the wind conditions. If more computational resources are available, one might apply a more sophisticated turbulence model in order to resolve the near-wall regions adequately. A physical model of the upper airway could be constructed with which, the flow could be studied in detail using flow visualization techniques. With a complete understanding of how the fluid mechanics within the upper airway causes the condition of DDSP, it might be possible to develop a treatment for this condition.

## **REFERENCES**

- 1. Parente, E.J., Martin, B.B., Tulleners, E.P., Ross, M.W., 2002, "Dorsal Displacement of the Soft Palate in 92 Horses During High-Speed Treadmill Examination (1993-1998)," Vet. Surg., 31, pp. 507-512.
- 2. Ducharme, N.G., Hackett, R.P., Woodie, J.B., Dykes, N., Erb, H.N., Mitchell, L.M., Solderholm, L.V., 2003, "Investigations into the role of the thyrohyoid muscles in the pathogenesis of dorsal displacement of the soft palate in horses," Equine Vet. J., 35, pp. 258-263.
- 3. Derksen, F.J., Holcombe, S.J., Hartmann, W., Robinson, N.E., Stick, J.A., 2001, "Spectrum Analysis of respiratory sounds in exercising horses with experimentally induced laryngeal hemiplegia or dorsal displacement of the soft palate," Am. J. Vet. Res., 62, pp. 659-664.
- 4. Martin, B.B., Reef, V.B., Parente, E.J., Sage, A.D., 2000, "Causes of poor performance of horses during training, racing, or showing: 348 cases (1992-1996)," J. Am. Vet. Med. Assoc., 216, pp. 554-558.
- 5. Duggan, V.E., MacAllister, C.G., Davis, M.S., 2002, "Xylazine-induced attenuation of dorsal displacement of the soft palate associated with epiglottic dysfunction in a horse," J. Am. Vet. Med. Assoc., 221, pp. 399-402.
- 6. Holcombe, S.J., Cornellisse, C.J., Berney, C., Robinson, N.E., 2002, "Electromyographic activity of the hyoepiglotticus muscle and control of epiglottis position in horses," Am. J. Vet. Res., 63, pp. 1617-1621.
- 7. Llewellyn, H.R., Petrowitz, A.B., 1997, "Sternothyroideus Myotomy for the Treatment of Dorsal Displacement of the Soft Palate," Proc. Am. Assoc. Equine Pract., 43, pp. 239-243.
- 8. Robinson, N.E., Sorenson, P.R., Goble, D.O., 1975, "Patterns of airflow in normal horses and horses with respiratory disease," Proc. Am. Assoc. Equine Pract., 21, 11-21
- 9. Rehder, R.S., Ducharme N.G., Hackett R.P., Nielan G.J., 1995, "Measurement of upper airway pressures in exercising horses with dorsal displacement of the soft palate," Am. J. Vet. Res., 56, pp. 269-274.
- 10. Kepler, G.M., Richardson, R.B., Morgan, K.T., Kimbell, J.S., 1998, "Computer Simulation of Inspiratory Nasal Airflow and Inhaled Gas Uptake in a Rhesus Monkey," Toxicology and App. Pharmacology, **150**, pp. 1-11.

- 11. Kimbell, J.S., Subramaniam, R.P., Gross, E.A., Schlosser, P.M., Morgan, K.T., 2001, "Dosimetry Modeling of Inhaled Formaldehyde: Comparison of Local Flux Predictions in the Rat, Monkey and Human Nasal Passages," Toxicological Sciences, 64, pp 100-110.
- 12. Anderson, J.D., Tulleners, E.P., Johnston, J.K., Reeves, M.J., 1995, "Sternothyrohyoideus myectomy or staphylectomy for treatment of intermittent dorsal displacement of the soft palate in racehorses: 209 cases (1986-1991)," J. Am. Vet. Med. Assoc., 206, pp. 1909-1912.
- 13. Lumsden, J.M., Derksen, F.J., Stick, J.A., Robinson, N.E., 1993, "Use of flow-volume loops to evaluate upper airway obstruction in exercising Standardbreds", 54, 5, pp 766-775.
- 14. Pope, B., 2000, Turbulent Flows, 1<sup>st</sup> ed., Cambridge University Press, Cambridge, U.K.
- 15. Lecture notes, "Turbulence Modeling and Simulation", fall 2007, Mechanical Engineering, MSU.
- 16. Fluent 6.2. User's Guide, 2005, Fluent Inc., Lebanon, New Hampshire, USA.

